Coupling the regional climate model ICON-CLM v2.6.6 into the Earth system model GCOAST-AHOI v2.0 using OASIS3-MCT v4.0

Ha Thi Minh Ho-Hagemann[1], Vera Maurer[2], Stefan Poll[3], Irina Fast[4]

[1]Institute of Coastal Research, Helmholtz-Zentrum Hereon, Geesthacht, Germany (Ha.Hagemann@hereon.de)

[2]Deutscher Wetterdienst, Offenbach, Germany

[3] Institute of Bio and Geosciences Agrosphere (IBG-3), Forschungszentrum Jülich, Jülich, Germany; CASA-SDL Terrestrial Systems, Jülich Supercomputing Centre (JSC), Jülich, Germany

[4]German Climate Computing Center (DKRZ), Hamburg, Germany

Correspondence to: Ha Thi Minh Ho-Hagemann, Ha.Hagemann@hereon.de

Abstract

Interactions and feedback between compartments of the Earth system can have a significant impact on local and regional climate and its changes due to global warming. These effects can be better represented by regional Earth system models (RESMs) than by traditional stand-alone atmosphere and ocean models. Here, we present the RESM GCOAST-AHOI version 2.0, which includes a new atmospheric component, the regional climate model ICON-CLM, which is coupled with the ocean model NEMO and the hydrological discharge model HD via the OASIS3-MCT coupler. The GCOAST-AHOI model has been developed and applied for climate simulations over the EURO-CORDEX domain. Two 11-year simulations from 2008-2018 of the uncoupled ICON-CLM and GCOAST-AHOI give similar results for seasonal and annual means of near-surface air temperature, precipitation, mean sea level pressure and wind speed at 10 m height. However, GCOAST-AHOI has a cold SST bias of 1-2 K over the Baltic and the North Seas, most pronounced in winter and spring seasons. A possible reason for the cold SST bias could be the underestimation of the downward shortwave radiation at the surface of ICON-CLM with the current model settings. Despite the cold SST bias, GCOAST-AHOI was able to capture other key variables such as those mentioned above well. Therefore, GCOAST-AHOI can be a useful tool for long-term climate simulations over the EURO-CORDEX domain. Compared with the stand-alone NEMO3.6 forced by ERA5 and ORAS5 boundary forcing, GCOAST-AHOI has positive biases in sea ice fraction and salinity, but negative biases in runoff, which need to be further investigated in the future to improve the coupled simulations. The new OASIS3-MCT coupling interface OMCI implemented in the ICON-CLM model adds a possibility to couple ICON-CLM with an external ocean model and an external hydrological discharge model using OASIS3-MCT instead of the YAC coupler. Using OMCI, it is also possible to set up a RESM with ICON-CLM and other ocean and hydrology models possessing the OASIS3-MCT interface for other regions, such as the Mediterranean Sea.

Keyword: GCOAST, ICON-CLM, OASIS3-MCT coupling interface, climate simulations, EURO-CORDEX, RESM

1   Introduction

GCOAST (Geesthacht Coupled cOAstal model SysTem) is an Earth system framework developed at Helmholtz-Zentrum Hereon, Germany (Staneva et al., 2018). GCOAST is a modular system of

4   different models each developed for a specific component of the Earth system. Based on a specific

5   scientific question, different models from GCOAST can be selected. These models can be plugged

6   together by various couplers, such as OASIS3-MCT (Craig et al., 2017), ESMF (Earth System Modeling

7   Framework; Hill et al., 2004), or FABM (Framework for Aquatic Biogeochemical Models;

8   https://fabm.net). The coupling can be done at different levels of coupling granularity and the

9   couplers handle the exchange of information between model combinations, individual models, and

10   processes.

11   GCOAST systems have been applied for several studies covering the Baltic and-North Sea region

12   and part of the North Atlantic. These studies include atmosphere-river-ocean-sea ice coupling (Ho-

13   Hagemann et al., 2020), atmosphere-wave coupling (Wahle et al., 2017; Wiese et al., 2019, 2020),

14   wave-ocean coupling (Staneva et al., 2016; Schloen et al., 2017; Lewis et al., 2019), hydrosphere-

15   biosphere coupling for the Elbe estuary (Pein et al., 2019), the total organic carbon-macrobenthos

16   coupling model (Zhang et al., 2019), and multi-model couplings developed by Lemmen et al. (2018),

17   which have been applied to assess ecosystem impacts of offshore wind farms (Slavik et al., 2019).

18   So far, the atmospheric model component of GCOAST has been the non-hydrostatic limited area

19   atmospheric model COSMO-CLM v5.0 (Rockel et al., 2008). The COSMO (cOnsortium for Small-scale

20   mOdeling) model was initially developed by the Deutscher Wetterdienst (DWD, the German

21   Meteorological Service) in the 2000s as a limited-area weather forecast model. Later, it was further

22   developed in the Climate Limited-area Modeling Community (CLM-Community) as the regional

23   climate model COSMO-CLM (hereafter referred to as CCLM). In December 2021, COSMO v6.0 was

24   released which is the last version of the COSMO model. With this release, the development of the

25   COSMO model ended after more than two decades. The successor of the COSMO model is the ICON

26   model.

27   In 2001, a cooperation between the DWD and the Max-Planck Institute for Meteorology (MPI-M)

28   was initiated, with the aim of developing a new modelling system for weather prediction and climate

29   simulations. As one result of this initiative, the global numerical weather prediction model ICON

30   (Icosahedral Nonhydrostatic) was developed (Zängl et al., 2015). Nowadays, with contributions from

31   the Karlsruhe Institute of Technology (KIT) and the German Climate Computing Center (DKRZ), etc.,

32   the ICON Earth system framework can include not only the atmospheric, land, river routing, ocean-

33   sea ice, wave, and biogeochemical compartments but also the Aerosols and Reactive Trace gases

34   (ART) model. ICON can be set up to operate on several high-performance computing systems such

35   as Bull ATOS at DKRZ (Hamburg, Germany), NEC-Aurora Tsubasa at DWD (Offenbach, Germany) or

36   BullSequana at Forschungszentrum Jülich (FZJ, Jülich, Germany). ICON can be used on a wide range

2

of scales from climate projection, climate prediction and numerical weather prediction down to large-eddy simulations (Dipankar et al., 2015; Heinze et al., 2017).

The atmospheric component of ICON includes two different physics packages: the first one is the Numerical Weather Physics package of DWD (i.e. the ICON-NWP model); and the second one is the ECHAM physics package of MPI-M (i.e. the ICON-A model, Giorgetta et al., 2018). The global atmospheric model ICON-A is coupled with the global ocean model ICON-O (Korn, 2017) and the land and biosphere model JSBACH (Reick et al., 2021) within the ICON Earth System Model (ICON-ESM; Jungclaus et al., 2022). ICON-NWP can be also coupled with ICON-O in the ICON-Seamless Earth system coupling framework which has been newly developed during the recent years. In ICON-Seamless, there are two options for the land surface schemes, TERRA and JSBACH, which are coupled via subroutine to the atmospheric component. A new land surface model (ICON-Land) is being developed based on JSBACH and some features of TERRA. Another component of ICON-Seamless is the wave model ICON-Wave. The hydrological discharge model HD can now be used as an external model instead of being coupled as a subroutine of JSBACH.

The components of ICON are coupled together using YAC (Yet Another Coupler; Hanke et al., 2016). However, coupling between ICON components, or the coupling of multiple ICON components to an external model without a YAC coupling interface is not supported due to how the initial communicator splitting is implemented.

ICON can also be used in a configuration with regional grid refinement (2-way nesting) or in limited area mode. ICON-LAM is the Limited-Area Mode of ICON-NWP. Starting in 2017, DWD and the CLM-Community decided to develop the climate limited area mode (ICON-CLM, Pham et al., 2021) based on ICON-LAM. Within ICON-Seamless, a limited area mode of the ocean model (ICON-O-LAM) is being developed and can be coupled with ICON-LAM via YAC.

As mentioned above, coupling a component or multiple components of ICON to an external model that has no YAC coupling interface is not supported and potentially impossible. For the coupling of ICON-CLM as an atmosphere component into GCOAST-AHOI, which includes HD and the ocean model NEMO (Nucleus for European Modelling of the Ocean, Madec et al. 2017), representing the ocean and sea ice components, basically, there were two feasible options: either to implement a YAC interface in NEMO and HD, or to implement an OASIS interface in ICON-CLM. For the option one, the YAC coupling interface was added into the HD source code by M. Hanke (DKRZ) (see Hagemann et al. 2023), but YAC has not yet been available in the NEMO source code. To our current knowledge, there is no RESM with NEMO using the YAC coupler. The NEMO model is already linked to the OASIS coupler, which has been used to couple NEMO with many other model components.

70 Implementing the YAC interface in NEMO would require a larger effort, as the NEMO source code is
71 much more complicated than the HD code. In addition, although the NEMO source code is freely
72 available, we are ordinary users in the NEMO community, not members of the model development
73 team. Therefore, implementing and especially maintaining the YAC interfaces in NEMO is a big
74 challenge. For the second option, HD and NEMO already have the OASIS3-MCT coupling interface
75 (OMCI), so all we had to do was to implement OMCI in ICON. Here, we also have the advantage that
76 we belong to the ICON development team of the CLM-Community, so that we can get great and
77 quick technical support from the development team when coding with ICON. Therefore, in 2021,
78 we started to port the OASIS coupling interfaces from CCLM to ICON-CLM for the coupling to NEMO
79 and HD.

80 Some other groups were using a similar method while coupling ICON into their available coupled
81 system model which does not include the YAC coupler. For example, Bauer et al. (2021) have
82 implemented the ESMF interfaces in an earlier version of ICON-NWP as well as into the ocean model
83 GETM to build up the regional ocean-atmosphere coupling over the Baltic Sea. However, they did
84 not consider sea ice in the coupling. There is an ongoing work at FZJ to couple ICON-CLM with the
85 Community Land Model (CLM) via the OASIS3-MCT coupler (manuscript in preparation) as has been
86 done for the CCLM via the OASIS interface (see Shrestha et al., 2014; Will et al., 2017).

87 The aim of this article is to give a detailed description of the OASIS3-MCT coupling interface
88 (hereafter referred to as OMCI) in ICON-CLM (ICON release version 2.6.6), how to implement OMCI
89 with as little modification of the ICON source code as possible, how to compile it on the high-
90 performance computing system Levante at DKRZ, and how to run the coupled system model
91 GCOAST-AHOI with ICON-CLM for climate simulations over the EURO-CORDEX domain. This
92 information is useful to other groups planning to couple ICON-CLM with NEMO or any other ocean
93 model that already has an OASIS3-MCT interface available. The Earth System Modelling (ESM)
94 Community agrees that ICON and IFS (coupled to FESOM and NEMO) will play a central role within
95 the Helmholtz Association of German Research Centres (HGF). This new OMCI opens more
96 opportunities to use ICON-CLM in ESM applications as well as in other modelling communities. The
97 OMCI can also be applied to couple with a land surface model with minor necessary adaptations.

98 We briefly introduce the coupled system model GCOAST-AHOI in Section 2 and describe the
99 details of OMCI in ICON-CLM in Section 3. Experiment setups are presented in Section 4, followed
100 by an analysis of the model simulations in Section 5. Finally, conclusions and a discussion are given
101 in Section 6.

2 The coupled system model GCOAST-AHOI

GCOAST-AHOI is a subset of GCOAST that includes model components for **A**-Atmosphere and Land, **H**-Hydrological discharge, **O**-Ocean, and **I**-Sea Ice. GCOAST-AHOI version 1.0 (Ho-Hagemann et al., 2020) contains the atmospheric model CCLM v5.0, the ocean model NEMO v3.6 (including the sea ice model LIM3) and the hydrological discharge model HD v4.0 (Hagemann and Dümenil, 1998; Hagemann et al., 2020), coupled via OASIS3-MCT v2.0. A detailed description of CCLM, NEMO and HD as components of GCOAST-AHOI can be found in Ho-Hagemann et al. (2020).

In the GCOAST-AHOI version 2.0, ICON-CLM replaces CCLM as atmospheric model, which is coupled to NEMO v3.6 and HD v5.1 via OASIS3-MCT v4.0. By coupling the atmosphere-ocean-river runoff models in GCOAST-AHOI, we aim to close the water balance in the RESM. Figure 1 illustrates the three models exchanging radiation, wind, pressure, temperature, humidity, water, and sea ice related variables at their interfaces via the OASIS coupler.

The OMCI in NEMO v3.6 has been modified compared to the original one in the officially released version at http://forge.ipsl.jussieu.fr/nemo/wiki/Users/release-3.6 to be able to receive state variables from the atmospheric model (Ho-Hagemann, 2024). Supplement S1 contains a flowchart of the OMCI for NEMO v3.6. This flowchart differs slightly from Figure 9 in Will et al. (2017), who used the older version NEMO v3.3. The OMCI in HD can be found in the source code publication of Hagemann and Ho-Hagemann (2021) and Hagemann et al. (2023). Supplement S2 shows the OMCI of HD. In this article, we describe in detail the OMCI in ICON-CLM.

In Section 3, we demonstrate the construction of the OMCI in ICON-CLM and the optional coupling methods between ICON-CLM and NEMO.

3 The coupling OASIS3-MCT interface in ICON

3.1 Interface structure

Figure 2 shows a flowchart of ICON with the OMCI implemented for coupling with NEMO and HD. 10 levels of ICON's source code are described: the first level is the main program ICON, the second level starts with the *start_mpi*, then *atmo_model* and ends with *stop_mpi*, etc.

Levels 2 to 6, 8 and 9 comprise subroutines of ICON (marked in red) that are modified by the coupling. On levels 3 to 7 and 10, new subroutines (orange boxes B1-B7) have been added with the OMCI. They are organized in three modules (cpl_oas_vardef.f90, cpl_oas_mpi.f90 and cpl_oas_interface.f90) containing about 3000 lines of Fortran code (including the current debug lines). The files have been added to the icon/externals/oasis3-mct directory and linked to the src/atm_phy_nwp directory of the ICON source tree. The detailed description of the interface

134 structure can be found in Supplementary S4.

135   Supplement S5 contains a guide for compiling ICON with this OMCI on Levante at DKRZ. The

136 preparation of OASIS input files for GCOAST-AHOI is described in Supplement S6, which is

137 accompanied by an example of the namcouple file in Supplement S7 and the namelist_cpl_atm_oce

138 in Supplement S8. The command to run GCOAST-AHOI on Levante is provided in Supplement S9.

139 The complete package to conduct experiments for this study is included in the Starter Package for

140 ICON-CLM Experiments (SPICE; Rockel and Geyer, 2022), which is a workflow engine to easily

141 perform long-term simulations. This tool has been further developed from the ICON-CLM_SP starter

142 package (Pham et al. 2021). Some additional parts for coupling with NEMO and HD have been added

143 to the original package.

3.2   Coupling methods

145 In the officially released version of NEMO v3.6, several fluxes and variables, including shortwave

146 (SW) and longwave (LW) radiation fluxes, latent (LH) and sensible heat (SH) fluxes, rain, snow,

147 evaporation, ice sublimation, mean sea level pressure (MSLP) and surface momentum, can be sent

148 from an atmospheric model to NEMO via the OASIS3-MCT coupler. To be able to receive state

149 variables from the atmospheric model, the OMCI in NEMO v3.6 has been modified to allow air

150 temperature and air specific humidity at 2 m height (T_2M and QV_2M respectively) to be sent from

151 the atmospheric model to NEMO. This allows NEMO to use these variables to calculate the LH and

152 SH, as in the case of the stand-alone NEMO using the "CORE bulk formulae" (Large and Yeager,

153 2004). Thus, we have three options for the coupling method between ICON and NEMO:

154   a) CPL_flx: **flux coupling**, which is the default option in the NEMO source code (described above)

155   b) CPL_var: **state variable coupling**, the new method, where SW and LW, T_2M, QV_2M, wind

156   speed at 10 m height (UV_10M), rain, snow, MSLP and surface momentum are sent from

157   ICON-CLM to NEMO. NEMO calculates LH and SH using the "CORE bulk formulae" which is

158   based on the Monin Obukhov similarity theory.

159   c) CPL_mix: **mixture coupling**, the new method, like CPL_var, but ICON-CLM also sends LH and

160   SH to NEMO. NEMO then averages them with the LH and SH calculated using the "CORE bulk

161   formulae".

162   With the modification of OMCI in NEMO v3.6, it is now easy to select the coupling method via

163 the namelist settings. Section 5 considers the simulations using the coupling method 3 (CPL_mix),

164 which was also used in Ho-Hagemann et al. (2020). An extra experiment using the coupling method

165 1 (CPL_flx) is also conducted and analyzed in Section 5.

166   In turn, NEMO sends the sea surface temperature, sea ice fraction and sea ice albedo to ICON-

167 CLM. Figure 3 illustrates how the surface temperature is updated in ICON over the ocean (left side)
168 and over land (right side) in the presence of sea ice and snow. ICON utilizes a tile approach to
169 compute surface fluxes of momentum and scalars. For the "sea-water type" grid boxes, the grid box
170 mean fluxes are computed as a weighted average of the fluxes over ice and over open water, using
171 the fractional ice cover *fice* and the fractional open water cover (*1 − fice*) as the respective weights.
172 Sea ice in each ICON grid box is considered only if *fice* exceeds its minimum value of 0.015.
173 Otherwise, the grid box is treated as ice-free. In ICON, two types of surface temperature are
174 considered: the ground temperature t_g and the surface temperature t_s. If a grid box is covered
175 by sea ice or snow, t_g is the mixed temperature of the free sea ice/free snow surface temperature
176 and the temperature on top of the sea ice/snow. Under the sea ice, t_s is calculated as a mixture of
177 the free sea ice temperature and the salt water freezing temperature of 271.45 K. If there is no sea
178 ice or snow in the grid box, t_g is equal to t_s. In principle, NEMO can send the mixed sea ice and
179 water temperature to ICON to update t_g over the ocean points, as in CCLM in Ho-Hagemann et al.
180 (2020). Or it can send the open water temperature, the sea ice surface temperature and the sea ice
181 fraction so that ICON can calculate t_g as the mixture. However, in the uncoupled mode of the
182 current ICON-CLM version, the sea surface temperature (SST) forcing is read in as the variable
183 t_seasfc (or t_s_w in Fig. 3) and passes through the subroutines *nwp_surface_init* and
184 *process_sst_and_seaice* to calculate t_g. To be consistent with the ICON-CLM updates, we pass the
185 SST (to update the t_seasfc), the sea ice fraction (to update fr_seaice), and the sea ice albedo
186 (alb_si_ext) from NEMO to ICON. ICON will then calculate t_g, t_s, alb_si, etc. using its sea ice
187 scheme. In the future, we may modify this coupling method by using the sea ice temperature from
188 NEMO.

4   Experimental design

190 In this study, four main experiments are conducted for the period of 2008-2018 (Table 2). The
191 uncoupled ICON (**ICON266**), the coupled GCOAST-AHOI (**ICPL266**), the stand-alone NEMO v3.6
192 (**NEMO3.6**), and the stand-alone HD v5.1 forced by ICON266 runoffs (**HDICON266**). Two additional
193 experiments are conducted: **ICPL266_noNewa** as a sensitivity test for the location of the Newa River
194 mouth on NEMO grid, and **ICPL266_flx** to test the coupling method CPL_flx.
195   Each experiment starts on 01 January 2008 and ends on 01 January 2019, restarting each month.
196 The integration domains of ICON, NEMO and HD are displayed in Fig. 4. The namelist setup of
197 physical parametrization for ICON-CLM is similar to that of the NUKLEUS project (B. Geyer, personal
198 communication). The resolution of ICON is R13B5, with an approximate mesh size of 12 km, using

199   60 vertical levels. The model top height is at 23.5 km. The following physical schemes are used in
200   the current namelist setting of ICON: Radiation scheme ecRad (Hogan and Bozzo, 2018; Rieger et
201   al., 2019); Mass-flux shallow and deep convection scheme (Tiedtke, 1989; Bechtold et al., 2008);
202   Microphysics single-moment scheme (Doms et al., 2004); Planetary boundary layer scheme
203   prognostic TKE (Raschendorfer, 2001; Raupach and Shaw, 1982); Land-surface scheme tiled TERRA
204   (Schrodin and Heise, 2001; Schulz et al., 2016; Schulz and Vogel, 2020). The initial and lateral
205   boundary forcing of ICON is obtained from the ERA5 reanalysis data (Hersbach et al., 2020). The
206   Tegen aerosol climatology (Tegen, 1997), i.e. a monthly aerosol optical depth of sulphate droplets,
207   total dust, organic carbon, black carbon, and sea salt, is used in this study. The initial and daily lateral
208   boundary forcing of NEMO is taken from the ORAS5 reanalysis data (Copernicus Climate Change
209   Service, 2021). The spatial resolution of NEMO is ~3.7 km with 50 vertical levels. In the stand-alone
210   mode, NEMO3.6 is driven by the atmospheric ERA5 data, the ocean ORAS5 data and climatological
211   river runoff data. HD has the resolution of 1/12 degrees, ca. 8 km. More information on the model
212   configuration can be found in Table 1 and in Ho-Hagemann et al. (2020).

213   To estimate the computational performance of the coupled model, we used LUCIA (Maisonnave
214   and Caubel, 2014), which is part of OASIS3-MCT. In Supplement S10 and Fig. S1, we describe how to
215   use LUCIA for GCOAST-AHOI to optimize the computational performance.

5   Evaluation of model simulations

217   The first two years 2008-2009 are excluded as spin-up time, and the output data of the two
218   simulations ICON266 and ICPL266 for nine years (2010-2018) are compared with the observational
219   and the ERA5 reanalysis data to assess the model performance. For sea surface temperature (SST),
220   we use the Operational Sea Surface Temperature and Ice Analysis (OSTIA) data (Good et al. 2020)
221   to evaluate the simulated SST of ICPL266. For air temperature at 2 m height (T_2M) and precipitation
222   (TOT_PREC), the daily E-OBS data (Haylock et al. 2008; Van den Besselaar et al. 2011) version 27.0
223   on the grid of 0.11 degree are used. The ERA5 reanalysis data are interpolated onto the E-OBS grid
224   and used as a reference for comparison with the simulated shortwave and longwave surface
225   radiation, turbulent fluxes, mean sea level pressure (PMSL), wind speed at 10 m height (SP_10M),
226   and T_2M. The Surface Radiation Data Set - Heliosat (SARAH) - Edition 2 (Pfeifroth et al. 2017) is
227   used to evaluate the shortwave downward radiation of the simulations.

228   Seasonal means of winter (DJF), spring (MAM), summer (JJA), autumn (SON) and annual means
229   (ANN) of several variables are analyzed in this section.

5.1 Sea surface temperature and 2m air temperature

Over the ocean, the sea surface temperature (SST) of ICON266 is the ERA5 forcing data, which is based on observations, so it's very close to the OSTIA data (not shown). Thus, the SST difference between the coupled and the stand-alone ICON-CLM simulations (Fig. S2) can be interpreted as a bias towards a measurement-based product. In the coupled model, the SST is provided by NEMO over the GCOAST domain. In general, ICPL266 has a cold SST bias of about 1-3 °C compared to OSTIA over the GCOAST domain, except around the British coast in summer (JJA, Fig. 5a). The SST bias of ICPL266_flx (Fig. 5b) is similar to ICPL266 (Fig. 5a). Ho-Hagemann et al. (2020) noted that using CPL_flx when coupling COSMO-CLM with NEMO leads to larger biases in the SST than using CPL_mix. This is not the case here when coupling ICON-CLM. A possible reason for this is that due to the tile approach (cf. Sect. 3.2), the fluxes from ICON-CLM to NEMO are sent separately over water and sea ice, while COSMO-CLM v5.0 doesn't have the tile approach, therefore, the fluxes in each ocean grid box sent from the atmosphere to the ocean are the mixed fluxes of water and sea ice.

The annual mean SST bias of the stand-alone NEMO3.6 is less than 0.5 °C over the Baltic and North Seas, and of about -1 to -2 °C over the North Atlantic compared to the OSTIA data (Fig. 5c). In summer, a positive SST bias of about 1-2 °C is present over the Baltic and North Seas. In this case, the reduction of SST by the coupling reduces the warm bias of the stand-alone NEMO3.6.

The cold SST bias of ICPL266 over the GCOAST domain intensifies the cold T_2M bias (Fig. 6b, Fig. S2b), especially in winter (DJF) and spring (MAM). In summer, ICPL266 reduces the warm T_2M bias of ICON266 (Fig. 6a). In general, the annual (ANN) T_2M bias of ICPL266 is slightly more negative by about 0.5 °C than that of ICON266. ICPL266_flx reproduces a similar T_2M (Fig. 6c) to that of ICPL266. Comparison with the E-OBS data (Fig. S3) shows similar results to Fig. 6, except over Northern Africa and Turkey, where the quality of the E-OBS data is affected by the lack of observations in that region (cf. Fig. 1 in Hagemann and Stacke, 2022).

5.2 Shortwave radiation, longwave radiation, and turbulent fluxes

A possible reason for the SST cold bias of ICPL266 may be that the shortwave and longwave radiation from ICON-CLM sent to NEMO is too low. Figure S4 shows the relative bias (%) of the shortwave downward radiation (SWDN) of ICON266 and ICPL266 compared to the ERA5 data, as well as the relative difference (%) between SARAH2 and ERA5. Figure 7 shows a zoomed section of Fig. S4 over the GCOAST ocean domain (note the adapted color scale). In general, both ICON266 and ICPL266 have a positive SWDN bias of less than 10 % over land compared to ERA5, except for the larger bias of 15-20 % over northern Europe in winter and eastern Europe in autumn (Fig. S4). Over the North Sea, ICON266 and ICPL266 have a small negative bias of about 5-10 % compared to ERA5 (Fig. 7).

263 The area of negative SWDN bias in the North Sea is slightly larger in ICPL266 than in ICON266.

264 Comparing the ERA5 data and the SARAH2 data, SWDN over southern Europe is similar between the

265 two datasets, with SARAH2 being slightly larger over land (Fig. S4). In general, the SWDN of ICON266

266 and ICPL266 over the North Sea is rather close to the SARAH2 data, but slightly overestimated over

267 the Baltic Sea.

268 Figure S5 in the Supplementary Appendix shows a similar plot to Fig. S4, but for the longwave

269 downward radiation (LWDN) and without the SARAH2 data, as it is not available. The modeled

270 LWDN has a negative bias of about 2-4 % annually and a larger bias in winter of about 6-8 %, most

271 pronounced over land. Over the ocean, ICON266 reproduces well the LWDN of the ERA5 data, and

272 ICPL266 has a small negative bias of 2-4 %. Overall, the negative SWDN bias over the North Sea and

273 the negative LWDN bias of ICON-CLM give an indication why the ICPL266 shows an increased cold

274 SST bias.

275 The ERA5 reanalysis data is used as the atmospheric forcing for the uncoupled NEMO3.6, and the

276 namelist settings of the NEMO model used in this study were tuned for an SST close to OSTIA (Fig.

277 5c). If the same namelist settings of NEMO3.6 are used for ICPL266, to reduce the cold SST bias over

278 the North Sea in the coupled simulations, a bias correction for SWDN and LWDN should be done.

279 Figures S6a, b and Figures S7 a, b show the seasonal SWDN and LWDN of ICPL266 and NEMO3.6

280 averaged over the North Sea and Baltic Sea for the period of 2010-2018. Note that we don't show

281 the result of ICPL266_flx in Figs. S6 and S7 because there is no output of LWDN in ICPL266_flx due

282 to the setup of the CPL_flx coupling method. Over the North Sea, the SWDN of ICPL266 is smaller

283 than the ERA5 used for NEMO3.6 in spring and summer (Fig. S6a), which mainly leads to the cold

284 SST bias of ICPL266 (Fig. 5a). Therefore, we plan to increase the SWDN of ICON by about 10 % before

285 sending it to NEMO. However, the cold SST bias over the Baltic Sea does not seem to be directly

286 related to the SWDN as there is no clear SWDN difference between ICPL266 and NEMO3.6 in

287 summer or in any other season (Fig. S6a). The LWDN of ICPL266 is similar to NEMO3.6 in summer

288 but slightly smaller in the other three seasons, both over the North Sea and the Baltic Sea. Increasing

289 the LWDN in ICON-CLM by about 5-10 W/m2 before sending it to NEMO should be tested to reduce

290 the SST bias. Note that the seasonal cycle of LWDN is more pronounced over the North Sea than

291 over the Baltic Sea.

292 We also compare the turbulent heat flux (i.e. the sum of SH and LH) of NEMO3.6 and the flux of

293 NEMO in ICPL266, averaged over the North Sea and the Baltic Sea (Fig. S6c and Fig. S7c), and the

294 net downward heat flux, which is the sum of SWDN, LWDN, SH and LH (Fig. S6d and Fig. S7d). We

295 only consider the turbulent flux because NEMO doesn't write out SH and LH separately, but only the

296 SWDN, LWDN and the net downward heat flux. Note that the turbulent flux from NEMO3.6 is

297 calculated using the "CORE bulk formulae", and due to the CPLmix coupling method used, the

298 turbulent flux in NEMO from ICPL266 is the average of the flux from ICON-CLM and the one

299 calculated inside NEMO (see section 3.2). The results are similar for both seas. The turbulent flux

300 and the net downward flux of the two experiments are quite similar with the largest differences in

301 winter (DJF) and summer (JJA).

302 Using ERA5 as a reference, the SH and LH biases of ICON266 and ICPL266 are shown in Fig. S8

303 and Fig. S9. Over land, the bias of ICON266 is very similar to that of ICPL266. However, over the

304 ocean, the bias of ICPL266 is generally more positive (i.e. the fluxes are less negative) than that of

305 ICON266 with the largest bias over the North Atlantic. Smaller heat fluxes are consistent with lower

306 SSTs in ICPL266, as lower SSTs lead to larger stability and less vertical mixing. Over the North and

307 Baltic Seas, SH and LH of ICPL266 are quite close to ERA5. Despite of the SST forcing from ERA5,

308 ICON266 has a negative SH bias of about -5 to -15 W/m^2 over the North and Baltic Seas, especially

309 in winter. This suggests a future analysis of the difference in air temperature at the lowest level of

310 ICON-CLM and ERA5.

311 Besides the energy flux biases causing the cold SST bias, a spin-up time of 2 years may be too

312 short for NEMO to reach the stable state, leading to the cold SST bias. In addition, NEMO's namelist

313 settings should also be optimized for the coupled simulations.

314 Currently, in the COPAT2 (Coordinated Parameter Testing, phase 2) initiative of the CLM-

315 Community, several parameters of ICON-CLM are being tested in a similar way as done for the

316 COSMO-CLM model (Russo et al., 2024) to find out the recommended settings. For example, the use

317 of the transient aerosol MAC2-SP (Kinne, 2019; Stevens et al., 2017) and a careful adjustment of

318 various namelist settings related to cloud cover, the soil and vegetation scheme and the turbulent

319 transfer will further reduce the T_2M cold bias and improve the shortwave downward radiation.

320 *5.3   Precipitation, mean sea level pressure, and wind speed*

321 The precipitation biases (Fig. 9) of the three simulations ICON266, ICPL266 and ICPL266_flx

322 compared to the E-OBS data are very similar in general, with a wet bias in winter and spring and a

323 dry bias in summer (JJA) and autumn (SON). Fig. S10 and Fig. S11 in the Supplementary show the

324 biases of PMSL and SP_10M of ICON266 and ICPL266 compared to ERA5. The PMSL and SP_10M

325 figures of ICPL266_flx are not shown because they are very similar to those of ICPL266.

326 ICPL266 tends to overestimate the PMSL throughout the year except in the summer, while

327 ICON266 has only a pronounced positive bias in winter (DJF) and negative bias in summer (JJA). The

328 wind speed of the two simulations is very similar over land (Fig. S11). ICPL266 reduces the wind

11

329 speed over the GCOAST ocean domain by up to 1.5 m s^{-1} compared to ICON266 (Figs. 8, S11).

330 Therefore, while ICON266 has a positive bias of about 0.5 m s^{-1} over the North Sea and the Baltic

331 Sea in winter (Fig. S11a), ICPL266 is very close to ERA5 (Fig. S11b). In general, ICPL266 produces a

332 cooler SST and weaker wind speed than ICON266, consistent with the smaller SH mentioned above

333 in Section 5.2. This positive feedback is known as the thermal feedback (TFB) mechanism in the

334 atmosphere-ocean surface coupling process (Zhang and Perrie, 2001; Renault et al., 2023).

335 Figure 10 shows monthly climatology of different variables (T_S, T_2M, TOT_PREC, PMSL) over

336 the GCOAST domain or the whole EURO-CORDEX domain, considering only ocean or land points.

337 ICPL266 has a cold T_S bias of about 1-2 $^{\circ}$C over the ocean (Fig. 10a), which also causes the T_2M

338 bias of 0.5-1 $^{\circ}$C over the ocean (Fig. 10c). In winter, ICPL266 is slightly colder over land than ICON266

339 and E-OBS (Fig. 10d). In summer, both simulations are very close to E-OBS. The simulated

340 precipitation of ICON266 tends to be overestimated compared to E-OBS with a maximum in May

341 and June, and slightly underestimated in August and September (Fig. 10b). The coupled run shows

342 1-3 mm/month less precipitation than the atmosphere-only experiment. In previous studies by Ho-

343 Hagemann et al. (2015, 2017), the stand-alone atmospheric model COSMO-CLM has a dry bias in

344 summer and the coupled run reduces the dry bias due to the improvement of the moisture

345 convergence and transport from ocean to land. This situation is not found in the current study,

346 which needs to be thoroughly analyzed in the future.

347 For the PMSL, the whole EURO-CORDEX domain is considered, but separately for ocean points

348 (Fig. 10e) and land points (Fig. 10f). In both cases, ICPL266 has a larger PMSL than ICON266. The

349 higher surface pressure in ICPL266 may be caused by the cooler air near the surface (due to the

350 negative T_2M bias) which leads to a higher density of the air mass and therefore a higher pressure.

351 Over the ocean, the PMSL of ERA5 is better reproduced by ICPL266 than by ICON266. Over land,

352 ICPL266 increases the PMSL positive bias in winter compared to ICON266. ICPL266_flx and ICPL266

353 have similar results (not shown) indicating that the coupling methods used in GCOAST-AHOI v2.0

354 don't affect the simulated climate variables strongly in this study.

355 *5.4 Sea ice*

356 The sea ice fraction bias of ICPL266 is about 0.2-0.3 over the Bothnian Bay and Sea in winter and

357 spring (Fig. 11a), while ICPL266_flx has a larger bias of about 0.3-0.5 (Fig. 11b) and the ERA5-forced

358 NEMO3.6 has a relatively small positive ice fraction bias there (Fig. 11c). The monthly mean sea ice

359 fraction averaged over the Bothnian Bay and Sea from ICPL266 and NEMO3.6 compared to the

360 OSTIA data is shown in Fig. 11d, where the sea ice temporal variation is quite well captured by the

361 two models, with a high peak in spring 2010 and a low peak in spring 2015. However, all three

362 simulations overestimate the sea ice fraction of OSTIA, with the two coupled simulations showing a

363 larger positive bias also in the time series. While ICPL266 has a winter SWDN about 8 % larger than

364 ERA5 (Fig. 7b), the incoming shortwave radiation is relatively small over the high latitudes in winter.

365 Therefore, we don't expect the positive SWDN bias to be the main reason for the overestimation of

366 sea ice. However, the LWDN of ICPL266 is about 10 W/m^2 lower than ERA5 (the forcing for

367 NEMO3.6) in winter over the North and Baltic Seas (Figs. S6b, S7b), and T_2M is about 3 $^{\circ}$C lower

368 than ERA5 over the Scandinavian region surrounding the Bothnian Bay and Sea (Fig. 6b). The cold

369 T_2M bias and negative LWDN bias of ICPL266 may explain its positive sea ice fraction bias. The cold

370 air temperature above the sea ice surface often produces more sea ice in winter and spring,

371 especially over an area with water of low salinity, such as the Bothnian Bay and Sea. Figure 6c shows

372 the larger T_2M cold bias of ICPL266_flx over the Baltic Sea in spring about 1°C more than ICPL266

373 (Fig. 6b) which is consistent with the larger sea ice fraction bias of ICPL266_flx (Fig. 11b) compared

374 with that of ICPL266 (Fig. 11a).

375   Another factor that could contribute to an increase in sea ice cover in spring would be an increase

376 in river runoff, which would result in less salty sea water and therefore more sea ice. These two

377 variables are analyzed in the next section.

378 ### 5.5 *Salinity and river runoff*

379 As mentioned in section 4, NEMO3.6 uses a climatological dataset for river runoff. Therefore, a

380 rough verification of the river runoff produced by the HD model in ICPL266 can be made by

381 comparing against this climatological river runoff. Differences in sea surface salinity and river runoff

382 between ICPL266 and NEMO3.6 are shown in Figure 12. The salinity simulated by ICPL266 is about

383 0.3-1 PSU higher than that of NEMO3.6 along the British Isles and the North Sea coast, and about

384 0.9-1.8 PSU higher in the Baltic Sea. Two areas with the largest salinity differences of more than 2

385 PSU are found south of the Kattegat and in the Gulf of Finland (Fig. 12a). The river runoff differences

386 (Fig. 12b) are largest near the Ems and Newa estuaries with more than 0.1 and 0.2 kg/m2/s,

387 respectively. The small river runoff difference between the two models at Kattegat cannot be used

388 to directly explain the increase in salinity there. The river runoff differences near the Ems estuary

389 have opposite signs (blue point overlaid by a red one in Fig. 12b), but very similar values. The reason

390 for this may be the discrepancy in the locations of river mouths between the NEMO3.6 setup, where

391 the river runoff is taken from a climatology, and those in ICPL266, which are defined based on the

392 river mouths in the HD model and the NEMO land-sea mask. In the latter case, the river mouths of

393 the HD model are interpolated onto the NEMO grid by searching for the closest ocean point of

394 NEMO. For example, the Ems River mouth in ICPL266 may not be in the same position as in the

395   climatology data. This discrepancy would lead to a difference in salinity near the coast (see Fig. 12a).

396   The extent of the effect on salinity in the deeper layers of the ocean in a longer-term simulation

397   needs to be analyzed in the future.

398   The large difference in river runoff near the Newa estuary is also caused by a mismatch in the

399   locations of the river mouths. In this case, the mouth of the Newa River in the climatology data

400   (60.1333°N, 29.888°E) is located slightly northwest of its "real" location (Wikipedia: 59.9453°N,

401   30.1708°E). The interpolation program used to define the mouths of the HD rivers on the NEMO

402   grid, by searching for the closest ocean point to the mouth of the HD rivers, found the mouth of the

403   Newa River at (59.95835°N, 30.20825°E), which is very close to the "real" position and at the

404   furthest grid point to the east in the Gulf of Finland. However, in the NEMO model, this eastern

405   boundary point in the Gulf of Finland is masked as a buffer zone. Therefore, the discharge from HD

406   to NEMO at this point in ICPL266_noNewa was ignored in the NEMO calculations, resulting in a lack

407   of freshwater inflow to the Gulf of Finland in ICPL266 (Fig. 12b2) and consequently an increase in

408   salinity (Fig. 12a2). The ICPL266 simulation with the Newa River mouth located on the NEMO buffer

409   zone is referred to ICPL266_noNewa in Figure 12. To overcome the location deficiency, that the

410   Newa River mouth was shifted one grid point to the west on the NEMO grid to allow the large

411   amount of river runoff to enter the Gulf of Finland in the coupled model. Therefore, the salinity

412   difference of ICPL266 compared to NEMO3.6 is reduced (Fig. 12a1) and the river runoff difference

413   shows the shift of the river mouth instead of the missing one (Fig. 12b1). The shift of the Newa River

414   mouth has little effect on the simulated atmospheric variables, but improves the simulated salinity

415   in the Baltic Sea, which is important for ecosystem modelling when a marine biogeochemical or

416   ecosystem model such as ECOSMO (Daewel and Schrum, 2013) is coupled with GCOAST-AHOI in the

417   future.

418   Other river mouths in the Baltic Sea have river runoff differences of less than 1.4 kg/m^2/s when

419   comparing ICPL266 to NEMO3.6. In general, ICPL266 tends to simulate less river runoff than the

420   climatology, leading to increased salinity there. The sources of the river runoff used for NEMO in

421   ICPL266 are the surface and sub-surface runoffs from the land component in ICON-CLM that are

422   transported to the ocean by HD. We applied the HD model to calculate the discharge using the

423   ICPL266 and ICON266 surface and subsurface runoff (Table 3) to evaluate it against the discharge

424   observation. The annual discharge difference of ICPL266 and HDICON266 in the Baltic Sea is about

425   -11 %. However, HDICON266 with a discharge of 12449 m^3/s is about -20 % biased towards the

426   HELCOM (Helsinki Commission; Svendsen and Gustafsson, 2022) value of 15676 m^3/s. Note that for

427   Baltic Sea ocean models, the mean long-term bias of river runoff must be less than 7 % (Hagemann

428   and Stacke, 2022). In the North Sea, ICPL266 discharge is about -4 % compared to HDICON266, which

429   has an annual value of 6366 m^3/s. However, both models have a dry discharge bias compared to the

430   OSPAR data (Farkas and Skarbøvik, 2021), which is 9190 m^3/s.

431   The main driver of the runoff is precipitation. Figure 9 shows that over Scandinavia, ICON266 has

432   a wet bias of about 10-30 mm/month in spring and summer compared to the E-OBS data. Thus, even

433   with the wet precipitation bias, ICON266 has a dry discharge bias. At the same time, ICPL266

434   precipitation is lower than for ICON266 in spring and summer, and therefore closer to the E-OBS

435   data (Fig. 9b). This difference in precipitation between ICPL266 and ICON266 explains the -11 %

436   difference in discharge, which increases the dry discharge bias. The reduction of the precipitation

437   bias in ICPL266 leading to a larger discharge dry bias implies that a better simulation of precipitation

438   compared to observations does not necessarily lead to a better runoff. We note that the runoff from

439   the atmosphere-only ICON-CLM has a general dry bias, which can be attributed to the respective

440   parametrizations in the TERRA land surface scheme used in ICON-CLM (S. Hagemann, pers.

441   communication, 2024). This dry discharge bias can be improved either by using the JSBACH land-

442   surface model in ICON-Seamless, or by applying a discharge bias correction developed by Hagemann

443   et al. (2024).

444   In Section 5.4, it was speculated that an increase in river runoff would lead to less saline sea

445   water and therefore more sea ice over the Baltic Sea. In our study, ICPL266 simulates too little river

446   runoff, leading to increased salinity in the Baltic Sea, which would mean less sea ice. However, the

447   sea ice fraction is increased compared to the ERA5-forced NEMO3.6. Thus, the main factor causing

448   the bias in the sea ice fraction seems to be the cold bias in the air temperature over sea ice in the

449   Baltic Sea in winter and spring (Fig. 6b and c).

Conclusion and Outlook

450

451   In the present study, we introduce the regional Earth system model (RESM) GCOAST-AHOI

452   version 2.0, in which a new atmospheric component - the regional climate model ICON-CLM version

453   2.6.6 - is coupled with the ocean model NEMO version 3.6 and the hydrological discharge model HD

454   version 5.1 via the OASIS3-MCT coupler version 4.0.

455   GCOAST-AHOI v2.0 is developed and applied for climate simulations over the EURO-CORDEX

456   domain. Several 11-year simulations from 2008-2018 of the uncoupled ICON-CLM (ICON266) and

457   GCOAST-AHOI (ICPL266, ICPL266_flx, ICPL266_noNewa) yield similar results for seasonal and annual

458   means of near-surface air temperature and precipitation, as well as mean sea level pressure and

459   wind speed at 10 m height. However, GCOAST-AHOI has a cold SST bias of 1-2 °C over the Baltic and

460   the North Seas, most pronounced in winter and spring seasons. The coupling methods CPL_mix and

461   CPL_flx give similar biases of SST and other climate variables like T_2M, precipitation, PMSL, etc.

462   A possible reason for the cold SST bias of GCOAST-AHOI could be the underestimation of the

463   downward shortwave radiation at the surface of ICON-CLM with the current model settings. A

464   deeper analysis of the bias will be done in the next study, especially after re-running the simulations

465   with the optimal settings of ICON-CLM, which will be found within the COPAT2 initiative of the CLM-

466   Community. For example, the performance of ICON-CLM will be tuned by using the transient

467   MACv2-SP aerosol data (Kinne, 2019) and modified namelist parameters related to cloud cover to

468   improve the shortwave downward radiation and reduce the cold bias.

469   Despite the cold SST bias, GCOAST-AHOI was able to capture the distribution of temperature,

470   precipitation, mean sea level pressure and wind speed well, similar to the uncoupled ICON-CLM

471   model. However, GCOAST-AHOI provides larger biases in sea ice fraction and salinity over the Baltic

472   Sea compared to the stand-alone ocean simulation (NEMO3.6) forced by ERA5 and ORAS5. The sea

473   ice fraction bias is related to the cold T_2M bias in ICPL266 and ICPL266_flx. Using the flux coupling

474   method CPL_flx instead of CPL_mix doesn't strongly affect the bias of SST and climate variables but

475   causes a larger sea ice fraction positive bias over the Baltic Sea. In the future study, a new simulation

476   of ICPL266 with the CPL_var coupling method will be conducted and compared with the current

477   ICPL266 and ICPL266_flx experiments to investigate the impact of the coupling methods on the sea

478   ice simulation.

479   The salinity bias is attributed to the dry runoff bias of ICPL266 compared to the climatology, with

480   the largest bias values are found near the Ems and Newa estuaries. The dry runoff bias near the Ems

481   and Newa River mouths is due to a mismatch of the river mouth locations between the climatology

482   and ICPL266. An adjustment of the Newa River mouth location must be made to allow the Newa

483   River runoff to flow into the Gulf of Finland. The effect of the river runoff bias on salinity in the

484   deeper layers of the ocean should be analyzed in the future.

485   In addition, added value of the coupled model compared to the stand-alone model is usually

486   found in the case of extreme events (Ho-Hagemann et al., 2015, 2017, 2020; Wiese et al., 2019,

487   2020). Therefore, we will analyze the model simulations with a focus on extreme events in the next

488   study.

489   Our present study shows that the RESM GCOAST-AHOI can be a useful tool for conducting long-

490   term regional climate simulations. The new OASIS3-MCT coupling interface OMCI implemented in

491   the ICON-CLM model adds a possibility to couple ICON-CLM with an external ocean model and an

492 external hydrological discharge model, not only with NEMO and HD, using OASIS3-MCT instead of

493 YAC. Given that the standalone model components for each the atmosphere and the ocean are

494 available for a specific geographical domain, it is also quite easy to apply GCOAST-AHOI to other

495 regions. Besides preparing the lateral boundary conditions for NEMO over the new domain, and the

496 OASIS input files (as described in Supplementary S6 and S7), it is necessary to prepare several new

497 parameter files so that OASIS3-MCT can exchange the discharge from HD to NEMO without

498 interpolation. On the one hand, these are files for the general setup of the HD model. The creation

499 of these files is described in Sect. 3 of the HD model readme mark down file included in the HD

500 model package (Hagemann et al. 2023). On the other hand, this includes the HD model coupling file,

501 which is used for coupling via OASIS. Instructions for its generation are provided in Section 2.1 of a

502 markdown file dedicated to the HD model coupling exercises (Hagemann et al. 2023).

503 ICON-CLM with OMCI is also used to couple ICON-CLM with NEMO v4.2 over the GCOAST domain

504 (manuscript in preparation) and with NEMO-MED v3.6 over the Mediterranean Sea region in the

505 CLM-Community. OMCI for the older ICON version 2.6.4 can be found in Ho-Hagemann (2022).

506 Recently, the ICON Consortium has developed and released the Community Interface (ComIn)

507 for the ICON model to allow ICON to be coupled with external model components. The main

508 challenge for the external model component coupling is the initial splitting of MPI_COMM_WORLD,

509 which is done in ICON by a grouping of the mpi communicators (MPI-handshake) (M. Hanke, pers.

510 communication, 2024). There are about 40 ComIn entry points in the new release version of ICON.

511 Using the ComIn entry points does not require any additional patching of the ICON source code. A

512 coupling interface to an external model such as OMCI would have to be moved into a ComIn-plugin

513 to connect to the entry points in the ICON source code. In addition, the communicator splitting using

514 the MPI-handshake algorithm would have to be implemented in the NEMO and HD source code.

515 Currently, also a limited area mode of the ocean model (ICON-O-LAM) is being developed within

516 the ICON consortium. This can be coupled with ICON-CLM via the YAC coupler in the ICON-Seamless

517 framework. When that RESM will be available in the future and will be applied for the EURO-CORDEX

518 domain, its simulation can be compared with the simulations of GCOAST-AHOI as a good reference.

519 Investigating difference in simulations of the two RESMs could be helpful to understand better the

520 coupling interactions and feedback between model components of the climate system.

521

the experiments and carried them out, analyzed the results; H.T.M. H.-H. prepared the manuscript with contributions from all co-authors; V.M. contributed to analyze the simulations; S.P contributed to develop the OMCI in ICON-CLM; I.F. supported debugging the GCOAST-AHOI on the DKRZ HPC system. All authors have read and agreed to the published version of the manuscript.

Code and data availability: ICON is available to the community under a permissive open source licence (BSD-3C). One can download the newest released version at https://gitlab.dkrz.de/icon/icon-model. The source code of ICON v2.6.6 including the OMCI is published on Zenodo (https://doi.org/10.5281/zenodo.11057794). Note that ICON v2.6.6 was released before the open source release of ICON. As this version still comprises 3rd party modules with a more restrictive license, we had to change the file access from public to available upon request.

The NEMO source code is freely available and distributed under CeCILL license (GNU GPL compatible). To download the NEMO reference version (for now revision 3.6):

svn co http://forge.ipsl.jussieu.fr/nemo/svn/NEMO/releases/release-3.6/NEMOGCM

The modified NEMO v3.6 source code for different coupling methods are published on Zenodo (https://doi.org/10.5281/zenodo.11057794).

The HD source code is available at https://doi.org/10.5281/zenodo.4893099.

562 Source code of OASIS3-MCT v4.0 with small modifications in lib/psmile/src/GPTLget_memusage.c and
563 lib/mct/mct/m_AttrVectComms.F90 is published on Zenodo (https://doi.org/10.5281/zenodo.11057794).

564 Input data, run-scripts, evaluation scripts are published on Zenodo (https://doi.org/10.5281/zenodo.11057794).
565 Because of its huge volume, forcing data used for this study is available from the authors upon request.

566 **Conflicts of Interest**: The authors declare no conflict of interest. The funders had no role in the design of the study; in
567 the collection, analyses, or interpretation of data; in the writing of the manuscript, or in the decision to publish the
568 results.

569

References

571 Bauer, T. P., Holtermann, P., Heinold, B., Radtke, H., Knoth, O., and Klingbeil, K.: ICONGETM v1.0 – flexible
572   NUOPC driven two-way coupling via ESMF exchange grids between the unstructured-grid atmosphere
573   model ICON and the structured grid coastal ocean model GETM, Geosci. Model Dev., 14, 4843–4863,
574   https://doi.org/10.5194/gmd-14-4843-2021, 2021.
575 Bechtold, P., Kohler, M., Jung, T., Leutbecher, M., Rodwell, M., Vitart, F., and Balsamo, G.: Advances in
576   predicting atmospheric variability with the ECMWF model, 2008: From synoptic to decadal time-scales.
577   Quart. J. Roy. Meteor. Soc., 134, 1337–1351, https://doi.org/10.1002/qj.289, 2008.
578 Copernicus Climate Change Service, Climate Data Store: ORAS5 global ocean reanalysis monthly data from
579   1958 to present, Copernicus Climate Change Service (C3S) Climate Data Store (CDS), https://doi.org/
580   10.24381/cds.67e8eeb7, 2021.
581 Craig, A., Valcke, S., and Coquart, L.: Development and performance of a new version of the OASIS coupler,
582   OASIS3-MCT_3.0, Geoscientific Model Development, 10, pp. 3297-3308, https://doi.org/10.5194/gmd-
583   10-3297-2017, 2017.
584 Daewel, U., and Schrum, C.: Simulating long-term dynamics of the coupled North Sea and Baltic Sea
585   ecosystem with ECOSMO II: Model description and validation. J. Marine Syst. 119–120, 30–49, 2013.
586 Dipankar, A., Stevens, B., Heinze, R., Moseley, C., Zängl, G., Giorgetta, M., and Brdar, S.: Large eddy simulation
587   using the general circulation model ICON, J. Adv. Model. Earth Syst., 7, 963–986,
588   doi:10.1002/2015MS000431, 2015.
589 Doms, G., and Coauthors: A description of the nonhydrostatic regional model LM. Part II: Physical
590   parameterization. Tech. Rep., Deutscher Wetterdienst, Offenbach, Germany, 146 pp.,
591   http://www.cosmo-model.org/content/model/documentation/core/cosmoPhysParamtr.pdf, 2004.
592 Farkas, C., and Skarbøvik, E.: OSPAR Contracting Parties' RID 2019 Data Report, NIBIO – Norwegian Institute
593   for Bioeconomy Research, 57 pp., 2021.
594 Giorgetta, M. A., Brokopf, R., Crueger, T., Esch, M., Fiedler, S., Helmert, J., et al.: ICON-A, the atmosphere
595   component of the ICON EarthSystem Model: I. Model description. Journal of Advances in Modeling Earth
596   Systems. https://doi.org/10.1002/2017MS001242, 2018.
597 Good, S., Fiedler, E., Mao, C., Martin, M.J., Maycock, A., Reid, R., Roberts-Jones, J., Searle, T., Waters, J.,
598   While, J., and Worsfold, M.: The Current Configuration of the OSTIA System for Operational Production of
599   Foundation Sea Surface Temperature and Ice Concentration Analyses. Remote Sens., 12, 720,
600   https://doi.org/10.3390/rs12040720, 2020.
601 Hagemann, S., and Dümenil, L.: A parametrization of the lateral waterflow for the global scale, Climate Dyn.,
602   14, 17–31, https://doi.org/10.1007/s003820050205, 1998.
603 Hagemann, S., and Ho-Hagemann, H.T.M.: The Hydrological Discharge Model - a river runoff component for
604   offline and coupled model applications (5.0.0), Zenodo. https://doi.org/10.5281/zenodo.4893099,
605   2021.Hagemann, S., Stacke, T., and Ho-Hagemann, H.T.M.: High resolution discharge simulations over
606   Europe and the Baltic Sea catchment, Frontiers in Earth Science, 8,
607   https://doi.org/10.3389/feart.2020.00012, 2020.
608 Hagemann, S., Stacke, T.: Complementing ERA5 and E-OBS with high-resolution river discharge over Europe.
609   Oceanologia 65: 230-248, doi:10.1016/j.oceano.2022.07.003, 2022.
610 Hagemann, S., Ho-Hagemann, H. T. M., and Hanke, M.: The Hydrological Discharge Model - a river runoff
611   component for offline and coupled model applications (5.2.2), Zenodo,

https://doi.org/10.5281/zenodo.10405875, 2023.

Hagemann, S., Nguyen, T. T., and Ho-Hagemann, H. T. M.: A three-part bias correction of simulated European river runoff to force ocean models, EGUsphere [preprint], https://doi.org/10.5194/egusphere-2024-1774, 2024.

Hanke, M., Redler, R., Holfeld, T., and Yastremsky, M.: YAC 1.2.0: new aspects for coupling software in Earth system modelling, Geosci. Model Dev., 9, 2755-2769, https://doi.org/10.5194/gmd-9-2755-201, 2016.

Haylock, M., Hofstra, N., Klein Tank, A., Klok, E., Jones, P., and New, M.: A European daily high-resolution gridded data set of surface temperature and precipitation for 1950–2006, J. Geophys. Res.-Atmos., 113, D20119, https://doi.org/10.1029/2008JD010201, 2008.

Heinze, R., Dipankar, A., Henken, C. C., Moseley, C., Sourdeval, O., Trömel, S., Xie, X., Adamidis, P., Ament, F., Baars, H., Barthlott, C., Behrendt, A., Blahak, U., Bley, S., Brdar, S., Brueck, M., Crewell, S., Deneke,H., Di Girolamo,P., Evaristo, R., Fischer, J., Frank, C., Friederichs, P., Göcke, T., Gorges, K., Hande, L., Hanke, M., Hansen, A., Hege, H-C., Hoose, C., Jahns, T., Kalthoff, N., Klocke, D., Kneifel, S., Knippertz, P., Kuhn, A., van Laar, T., Macke, A., Maurer, V., Mayer, B., Meyer, C. I., Muppa, S. K., Neggers, R. A. J., Orlandi, E., Pantillon, F., Pospichal, B., Röber,N., Scheck, L., Seifert, A., Seifert, P., Senf, F., Siligam, P., Simmer, C., Steinke, S., Stevens, B., Wapler, K., Weniger, M.,Wulfmeyer, V., Zängl, G., Zhang, D., and Quaas, J.: Large-eddy simulations over Germany using ICON: A comprehensive evaluation, Q. J. Roy. Meteor. Soc., 143, 69–100, 2017.

Hersbach, H., Bell, B., Berrisford, P., Hirahara, S., Horányi, A., Muñoz Sabater, J., et al.: The ERA5 global reanalysis, Q. J. Roy. Meteor. Soc., 146(730), 1999-2049. https://doi.org/10.1002/qj.3803, 2020.

Hill, C., DeLuca, C., Balaji, Suarez, M., and Da Silva, A.: The architecture of the Earth System Modeling Framework, Computing in Science Engineering, 6, 18–28, https://doi.org/10.1109/MCISE.2004.1255817, 2004.

Hogan, R. J., and Bozzo, A.: A flexible and efficient radiation scheme for the ECMWF model. J. Adv. Model Earth Sys., 10(8), 1990–2008, 2018.

Ho-Hagemann, H. T. M.: The OASIS3-MCT Coupling Interface for ICON-CLM (1.0.0). Zenodo. https://doi.org/10.5281/zenodo.5833118, 2022.

Ho-Hagemann, H. T. M.: Regional Earth system model GCOAST-AHOI v2.0 with ICON-CLM (1.0.1). Zenodo. https://doi.org/10.5281/zenodo.11057794, 2024.

Ho-Hagemann, H. T. M., Hagemann, S., and Rockel, B.: On the role of soil moisture in the generation of heavy rainfall during the Oder flood event in July 1997, Tellus A 2015, 67, 28661, https://doi.org/10.3402/tellusa.v67.28661, 2015.

Ho-Hagemann, H. T. M., Gröger, M., Rockel, B., Zahn, M., Geyer, B., and Meier, H. E. M.: Effects of air-sea coupling over the North Sea and the Baltic Sea on simulated summer precipitation over Central Europe, Clim Dyn 49, 3851-3876. https://doi.org/10.1007/s00382-017-3546-8, 2017.

Ho-Hagemann, H. T. M., Hagemann, S., Grayek, S., Petrik, R., Rockel, B., Staneva, J., Feser, F., and Schrum, C.: Internal model variability of the regional coupled system model GCOAST-AHOI, Atmosphere, 11(3), 227. https://doi.org/10.3390/atmos11030227, 2020.

Jungclaus, J. H., Lorenz, S. J., Schmidt, H., Brovkin, V., Brüggemann, N., Chegini, F., et al.: The ICON Earth System Model version 1.0. Journal of Advances in Modeling Earth Systems, 14, e2021MS002813. https://doi.org/10.1029/2021MS002813, 2022.

Kinne, S.: Aerosol radiative effects with MACv2, Atmos. Chem. Phys., 19, 10919–10959, https://doi.org/10.5194/acp-19-10919-2019, 2019.

Korn, P.: Formulation of an unstructured grid model for global ocean dynamics. Journal of Computational Physics, 339, 525–552. https://doi.org/10.1016/j.jcp.2017.03.009, 2017.

Large, W. G., and S. Yeager: Diurnal to decadal global forcing for ocean and sea-ice models: the data sets and flux climatologies, NCAR Technical Note, NCAR/TN-460+STR, CGD Division of the National Center for Atmospheric Research, 2004.

Lewis, H.W., Castillo Sanchez, J.M., Siddorn, J., King, R.R., Tonani, M., Saulter, A., Sykes, P., Pequignet, A.-C., Weedon, G.P., Palmer, T., Staneva, J., and Bricheno, L.: Can wave coupling improve operational regional ocean forecasts for the north-west European Shelf?, Ocean Sci., 15, 669-690, https://doi.org/10.5194/os-15-669-2019, 2019.

Lemmen, C., Hofmeister, R., Klingbeil, K., Nasermoaddeli, M.H., Kerimoglu, O., Burchard, H., Kösters, F., and Wirtz, K.W.: Modular System for Shelves and Coasts (MOSSCO v1.0) – a flexible and multi-component

framework for coupled coastal ocean ecosystem modelling, Geosci. Model Dev., 11, 915-935, https://doi.org/10.5194/gmd-11-915-2018, 2018.

Madec, G., Bourdallé-Badie, R., Bouttier, P.-A., Bricaud, C., Bruciaferri, D., Calvert, D., Chanut, J., Clementi, E., Coward, A., Delrosso, D., Ethé, C., Flavoni, S., Graham, T., Harle, J., Iovino, D., Lea, D., Lévy, C., Lovato, T., Martin, N., Masson, S., Mocavero, S., Paul, J., Rousset, C., Storkey, D., Storto, A., and Vancoppenolle, M.: NEMO ocean engine (Version v3.6-patch), Tech. rep., Pôle De Modélisation De L'institut Pierre-simon Laplace (IPSL), Zenodo, https://doi.org/10.5281/ZENODO.3248739, 2017.

Maisonnave E., and Caubel A.: LUCIA, load balancing tool for OASIS coupled systems, https://cerfacs.fr/wp-content/uploads/2018/10/GLOBC_TR_Maisonnave_lucia_arnaud_2014.pdf, 2014.

Pein, J., Eisele, A., Hofmeister, R., Sanders, T., Daewel, U., Stanev, E.V., van Beusekom, J., Staneva, J., and Schrum, C.: Nitrogen cycling in the Elbe estuary from a joint 3D-modelling and observational perspective, Biogeosciences Discuss., (July), 1–34, https://doi.org/10.5194/bg-2019-265, 2019.

Pfeifroth, U., Kothe, S., Müller, R., Trentmann, J., Hollmann, R., Fuchs, P., and Werscheck, M.: Surface Radiation Data Set – Heliosat (SARAH) – Edition 2, Satellite Application Facility on Climate Monitoring, https://doi.org/10.5676/EUM_SAF_CM/SARAH/V002, 2017.

Pham, T. V., Steger, C., Rockel, B., Keuler, K., Kirchner, I., Mertens, M., Rieger, D., Zängl, G., and Früh, B.: ICON in Climate Limited-area Mode (ICON release version 2.6.1): a new regional climate model, Geosci. Model Dev., 14, 985–1005, https://doi.org/10.5194/gmd-14-985-2021, 2021.

Raupach, M.R., and Shaw, R.H.: Averaging procedures for flow within vegetation canopies. Boundary-Layer Meteorol 22, 79–90. https://doi.org/10.1007/BF00128057, 1982.

Raschendorfer, M.: The new turbulence parameterization of LM. In: G. Doms and U. Schättler (Edts.): COSMO Newsletter No. 1, 89-97 (available at www.cosmo-model.org), 2001.

Reick, C., V. Gayler, D. Goll, and S. Hagemann et al.: JSBACH 3 - The land component of the MPI Earth System Model: Documentation of version 3.2, Berichte zur Erdsystemforschung, 240, Max Planck Institute for Meteorology, Hamburg, http://doi.org/10.17617/2.3279802, 2021.

Renault, L., Masson, S., Oerder, V., Colas, F., and McWilliams, J.C.: Modulation of the oceanic mesoscale activity by the mesoscale thermal feedback to the atmosphere, J. Phys. Oceanogr., 53, pp. 1651-1667, 10.1175/JPO-D-22-0256.1, 2023.

Rieger, D., Köhler, M., Hogan, R., Schäfer, S., Seifert, A., Lozar, A. D., and Zängl, G.: ecRad in ICON – Implementation Overview, Reports on ICON, Deutscher Wetterdienst, Offenbach, Germany, https://doi.org/10.5676/DWDpub/nwv/icon004, 2019.

Rockel, B., and Geyer, B.: SPICE (Starter Package for ICON-CLM Experiments) (2.1), Zenodo. https://doi.org/10.5281/zenodo.7298390, 2022.

Rockel, B., Will, A., and Hense, A.: The regional climate model COSMO-CLM (CCLM), Meteorol. Z. 2008, 17, 347–348. doi:10.1127/0941-2948/2008/0309, 2008.

Russo, E., Geyer, B., Petrik, P., Keuler, K., Adinol, M., Feldmann, H., Goergen, K., Kerkweg, A., Khain, P., Ludwig, P., Mertens, M., Pothapakula, P., Raffa, M., Rockel, B., Schulz, J.-P., Sulis, M., Ho-Hagemann, H. T. M., Truhetz, H., Uzan, L., Voggenberger, U., and Steger, C.: CLM Community WG EVAL, COordinated Parameter Testing project 2 (COPAT2): COSMO-CLM 6.0 clm1 recommended model configuration, COSMO Technical Reports, No. 51, https://doi.org/10.5676/DWD_pub/nwv/cosmo-tr_51, 2024.

Schloen, J., Stanev, E.V., and Grashorn, S.: Wave-current interactions in the southern North Sea: The impact on salinity. Ocean Modelling 111 (2017) 19–37, https://doi.org/10.1016/j.ocemod.2017.01.003, 2017.

Schrodin, R., and Heise, E.: The multi-layer-version of the DWD soil model TERRA/LM. Consortium for Small-Scale Modelling (COSMO) Tech. Rep., 2, 16, 2001.

Shrestha, P., Sulis, M., Masbou, M., Kollet, S., and Simmer, C.: A scale-consistent terrestrial systems modeling platform based on COSMO, CLM, and ParFlow, Mon. Weather Rev., 142, 3466–3483, 2014.

Schrodin, R., and Heise, E.: The multi-layer-version of the DWD soil model TERRA/LM. Consortium for Small-Scale Modelling (COSMO) Tech. Rep 2001, 2, 16, 2001.

Schulz, J.-P., Vogel, G., Becker, C., Kothe, S., Rummel, U., Ahrens, B.: Evaluation of the ground heat flux simulated by a multi-layer land surface scheme using high-quality observations at grass land and bare soil Meteorol. Z., 25, pp. 607-620, https://doi.org/10.1127/metz/2016/0537, 2016.

Schulz, J.-P., and Vogel, G.: Improving the processes in the land surface scheme TERRA: bare soil evaporation and skin temperature Atmosphere, 11, p. 513, https://doi.org/10.3390/atmos11050513, 2020.

Slavik, K., Lemmen, C., Zhang, W., Kerimoglu, O., Klingbeil, K., and Wirtz, K.W. The large scale impact of

720   offshore windfarm structures on pelagic primary production in the southern North Sea, Hydrobiologia
721   (2019) 845: 35, https://doi.org/10.1007/s10750-018-3653-5, 2019.

722 Staneva, J., Alari, V., Breivik, Ø., Bidlot, J.-R., and Mogensen, K.: Effects of wave-induced forcing on a
723   circulation model of the North Sea, Ocean Dynamics, https://doi.org/10.1007/s10236-016-1009-0, 2016.

724 Staneva, J., Schrum, C., Behrens, A., Grayek, S., Ho-Hagemann, H., Alari, V., Breivik, Ø., and Bidlot, J.-R.: A
725   North Sea - Baltic Sea regional coupled models: atmosphere, wind, waves and ocean. In: Buch, E.,
726   Fernández, V., Eparkhina, D., Gorringe, P., and Nolan, G. (Eds.): Operational Oceanography serving
727   Sustainable Marine Development, Proceedings of the Eight EuroGOOS International Conference, 516 pp,
728   ISBN 978-2-9601883-3-2, 2018.

729 Stevens, B., Fiedler, S., Kinne, S., Peters, K., Rast, S., Müsse, J., Smith, S. J., and Mauritsen, T.: MACv2-SP: a
730   parameterization of anthropogenic aerosol optical properties and an associated Twomey effect for use in
731   CMIP6, Geosci. Model Dev., 10, 433–452, https://doi.org/10.5194/gmd-10-433-2017, 2017.

732 Svendsen, L. M. and Gustafsson, B.: Waterborne nitrogen and phosphorus inputs and water flow to the Baltic
733   Sea 1995-2018. https://helcom.fi/baltic-sea-trends/environment-fact-sheets/eutrophication/, 2022.

734 Tegen, I., P. Hollrigl, M. Chin, I. Fung, D. Jacob, and Penner, J.: Contribution of different aerosol species to the
735   global aerosol extinction optical thickness: Estimates from model results, J. Geophys. Res., 102, 23895-
736   23915, 1997.

737 Tiedtke, M. A comprehensive mass flux scheme for cumulus parameterization in large-scale models. Mon.
738   Weather Rev. 1989, 117, 1779–1800.

739 Van den Besselaar, E., Haylock, M., Van der Schrier, G., and Klein Tank, A.: A European daily high-resolution
740   observational gridded data set of sea level pressure, J. Geophys. Res.-Atmos., 116, D11110,
741   https://doi.org/10.1029/2010JD015468, 2011.

742 Wahle, K., Staneva, J., Koch, W., Fenoglio-Marc, L., Ho-Hagemann, H.T.M., and Stanev, E.V.: An atmosphere–
743   wave regional coupled model: improving predictions of wave heights and surface winds in the southern
744   North Sea, Ocean Sci., 13, 289-301, https://doi.org/10.5194/os-13-289-2017, 2017.

745 Wiese, A., Staneva, J., Ho-Hagemann, H. T. M., Grayek, S., Koch, W., and Schrum, C.: Internal Model Variability
746   of Ensemble Simulations with a Regional Coupled Wave-Atmosphere Model GCOAST, Frontiers in Marine
747   Science, 7, 596843, https://doi.org/10.3389/fmars.2020.596843, 2020.

748 Wiese, A., Stanev, E., Koch, W., Behrens, A., Geyer, B., and Staneva, J.: The Impact of the Two-Way Coupling
749   between Wind Wave and Atmospheric Models on the Lower Atmosphere over the North Sea, Atmosphere
750   2019, 10, 386, https://doi.org/10.3390/atmos10070386, 2019.

751 Will, A., Akhtar, N., Brauch, J., Breil, M., Davin, E., Ho-Hagemann, H.T.M., Maisonnave, E., Thürkow, M., and
752   Weiher, S.: The COSMO-CLM 4.8 regional climate model coupled to regional ocean, land surface and
753   global earth system models using OASIS3-MCT: Description and performance, Geosci. Model Dev. 2017,
754   10, 1549–1586. doi:10.5194/gmd-10-1549-2017, 2017.

755 Zängl, G., Reinert, D., Rípodas, P., and Baldauf, M.: The ICON (ICOsahedral Non-hydrostatic) modelling
756   framework of DWD and MPI-M: Description of the non-hydrostatic dynamical core, Q. J. Roy. Meteor.
757   Soc., 141, 563–579, https://doi.org/10.1002/qj.2378, 2015.

758 Zhang, Y. and Perrie, W.: Feedback Mechanisms For The Atmosphere And Ocean Surface, Boundary-Layer
759   Meteorology 100, 321–348. https://doi.org/10.1023/A:1018996505248, 2001.

760 Zhang, W., Wirtz, K., Daewel, U., Wrede, A., Kröncke, I., Kuhn, G., Neumann, A., Meyer, J., Ma, M., and
761   Schrum, C.: The budget of macrobenthic reworked organic carbon - a modelling case study of the North
762   Sea, Journal of Geophysical Research-Biogeosciences, https://doi.org/10.1029/2019JG005109, 2019.

763

Table 1: Model configuration

Configuration	ICON	NEMO	HD	Coupler OASIS3-MCT
Version	v2.6.6	v3.6	v5.1	v4.0
Domain	EURO-CORDEX	North Sea, Baltic Sea, North Atlantic	Europe	-
Resolution	~ 12 km	~ 3.7 km	~ 8 km	-
Grid points	231660	902 x 777	960 x 540	
Time step	100 s	90 s	3600 s	3600 s
Forcing	ERA5	ORAS5, OTIS	-	-

764

Table 2: Model experiments

Experiment	Description
ICON266	Uncoupled ICON-CLM v2.6.6 forced by ERA5
ICPL266	Coupled GCOAST-AHOI forced by ERA5 and ORAS5
ICPL266_noNewa	Coupled GCOAST-AHOI forced by ERA5 and ORAS5, Newa River mouth is located on the buffer zone of NEMO grid.
ICPL266_flx	Coupled GCOAST-AHOI forced by ERA5 and ORAS5, coupling method CPL_flx
NEMO3.6	Stand-alone NEMO v3.6 forced by ERA5 and ORAS5
HDICON266	Stand-alone HD v5.1 forced by surface runoff and sub-surface runoff of ICON266

765
766

Table 3: Seasonal discharge (m^3/s) of ICPL266 and HDICON266 summed over the North Sea, the Baltic Sea during the period of 2010-2018. Diff. (%) is the difference of ICPL266 to HDICON266.

Areas	North Sea			Baltic Sea		
Seasons	ICPL266	HDICON266	Diff. (%)	ICPL266	HDICON266	Diff. (%)
DJF	7356	7687	-3.31	9148	10864	-15.80
MAM	6896	7438	-5.42	18788	19884	-5.51
JJA	5103	5482	-3.79	9837	10990	-10.49
SON	4352	4857	-5.05	6755	8056	-16.15
ANN	5927	6366	-4.39	11132	12449	-10.58

767

768

Figure 1: Model components of GCOAST-AHOI and variables exchanged via the OASIS3-MCT coupler. Two solid arrows display the communication between atmosphere-land (yellow-green arrow) and ocean-sea ice (gray-blue arrow), which is done via subroutines inside ICON-CLM and NEMO, respectively. Dotted arrows show the transfer between components via the OASIS interface. Yellow arrows present atmospheric transfer to ocean-sea ice and river runoff. The cyan arrow shows the discharge from the river to the ocean. Blue arrows demonstrate the transfer of sea surface temperature (SST) from the ocean as well as the sea ice albedo and sea ice fraction to the atmosphere.

Figure 2 (flowchart):

L1 ICON

L2 start_mpi   atmo_model   stop_mpi

L3 B1 cpl_oas_init   construct_atmo_model   B2 construct_atmo_coupler_OAS   atmo_nonhydrostatic   destruct_atmo_model

L4 …; read_atmo_namelists
configure_run; configure_initicon;
set_mpi_work_communicators;
detachRestartProcs;
prefetch_main_proc;
name_list_io_main_proc;
build_decomposition; configure_*

oasis_set_couplcomm;
cpl_oas_vardef;
cpl_alloc_meteofields;
read_namelist_oasis;
cpl_oas_define;
define_mask_cpl

construct_atmo_nonhydrostatic   **perform_nh_stepping**   destruct_atmo_nonhydrostatic

L5 B3 oasis_set_couplcomm;
oasis_enddef

configure_atm_phy_nwp;
construct_nwp_phy_state;
construct_nwp_lnd_state;
init_icon; construct_nh_state;
configure_io; …

init_nwp_phy;
set_sst_and_seaice;
init_slowphysics;
perform_nh_timeloop;
deallocate_nh_stepping $ktstep=nsteps\_total$

L6 $ktstep=0$ B4 cpl_oas_receive $0 < ktstep \le nsteps\_total$

…; read_latbc_data_sync; update_nwp_phy_bcs;
cpl_oas_receive;
process_sst_and_seaice; ...
integrate_nh; ...
cpl_oas_send;
nwp_diag_for_output; nwp_opt_diagnostics, … $timeloop$ B6 destruct_atmo_coupler_OAS;
cpl_oas_finalize

L7 oasis_get   B5 oasis_send   nwp_nh_interface

L8-9 **nwp_turbtrans:** _surface; _turbdiff;
_microphysics; _convection; cover_koe;
nwp_radiation; …, _statistics   **nwp_turbtrans: turbtran**

L10 B7 cpl_oas_physc_tend

769

Figure 2: Flowchart of ICON-NWP/ICON-CLM with the OASIS3-MCT coupling interface OMCI. The running sequence is from top to bottom, and from left to right. "L1" indicates the Level 1 – main program ICON, etc. At the levels 2 to 6, 8 and 9, subroutines (in red text) of ICON are modified by the coupling. At the levels 3 to 7 and 10, subroutines added for OMCI are shown in orange boxes (B1-B7).

Figure 3 (diagram):

SST data

t_seasfc

Sea ice scheme

OCEAN   LAND

t_g   t_g   (Top of snow) t_g $\sum$ t_g_tk (Top of snow)   t_g

t_g_ti (Top of ice)   t_g   t_g_t3

t_g_tw

(Ice-free)   (Snow-free)

t_s   t_s_t1   t_s   t_s_t3

t_s $\sum$ t_s_tk (Under snow)   t_s_t5   t_s_t2

t_s_ti (Under ice)   t_s   t_s_t3   t_s_t4

t_s_tw

Open water   Sea ice   Snow   Land tiles

TILE APPROACH $t\_g = t\_g\_ti * fice + t\_g\_tw (1 - fice)$
$t\_s = t\_s\_ti * fice + t\_s\_tw (1 - fice)$

$t\_g = \sum_{k=1}^{ntiles} a_k * t\_g\_t_k$ $t\_s = \sum_{k=1}^{ntiles} a_k * t\_s\_t_k$

t_g_tw=t_g_t (isub_water) ; t_g_ti =t_g_t (isub_seaice)
t_s_tw=t_s_t (isub_water) ; t_s_ti =t_s_t (isub_seaice)

770

Figure 3: Surface temperature exchange between atmosphere and ocean/land in ICON and GCOAST-AHOI.

25
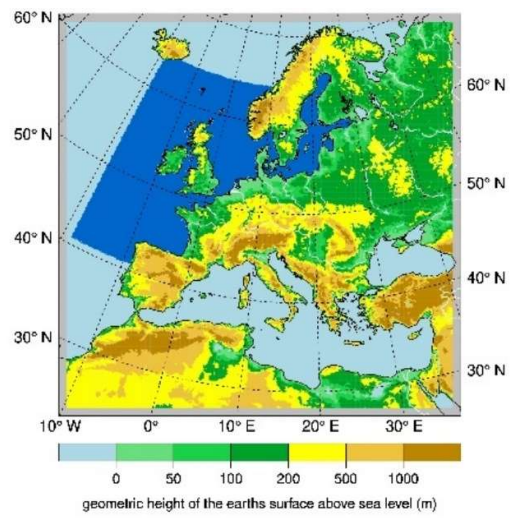
771

Figure 4: Integration domains of ICON and HD (EURO-CORDEX) and of NEMO-LIM3 (dark blue).

772

773   a) ICPL266
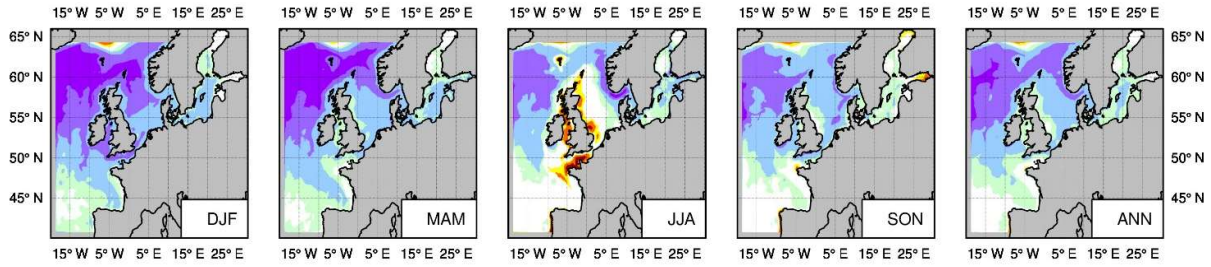
774
775   b) ICPL266_flx
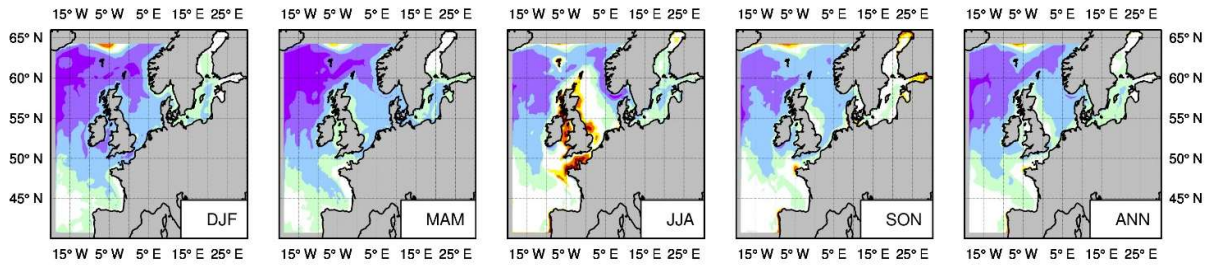
776
777   c) NEMO3.6
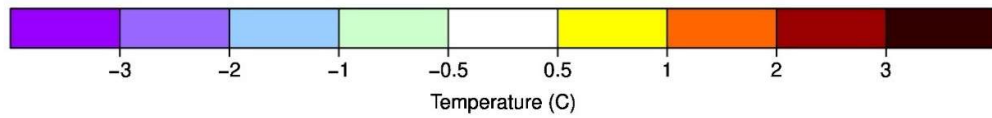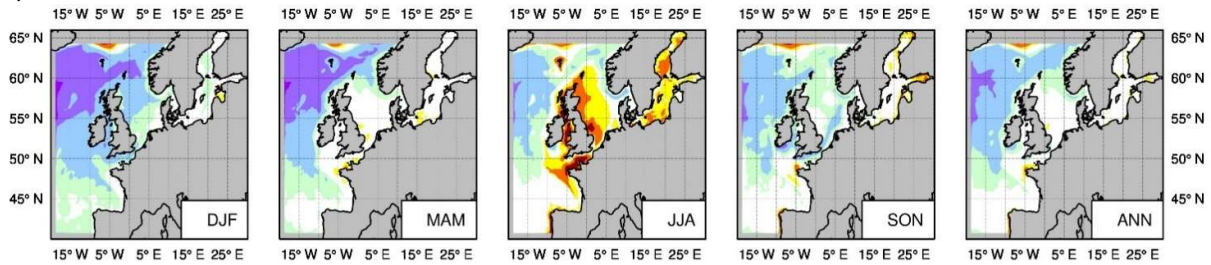
778

Figure 5: Seasonal (DJF, MAM, JJA, SON) and annual (ANN) mean of sea surface temperature (K) bias of a) ICPL266, b) ICPL266_flx and c) NEMO3.6 with respect to the OSTIA data for the period of 2010-2018 over the GCOAST domain.
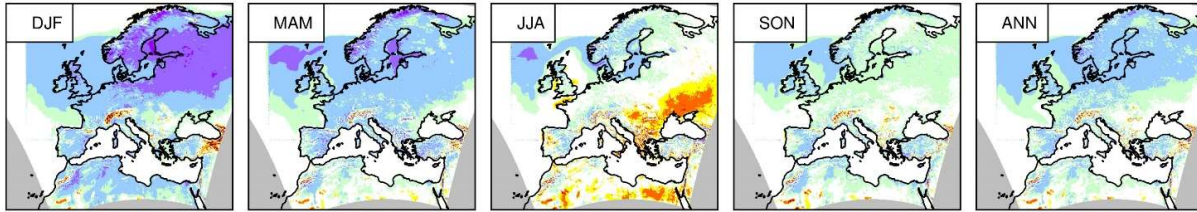
779
780

781   a) ICON266

782
783   b) ICPL266

784
785   c) ICPL266_flx

786
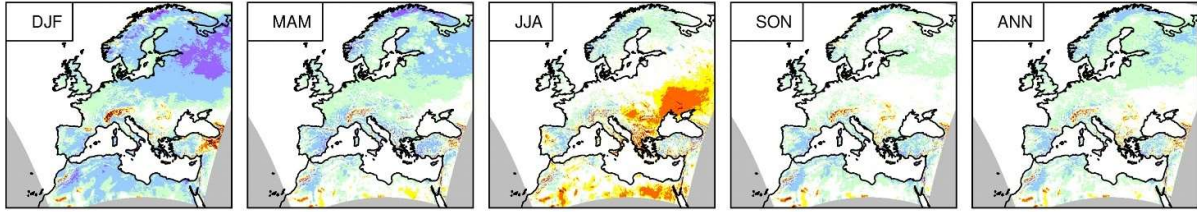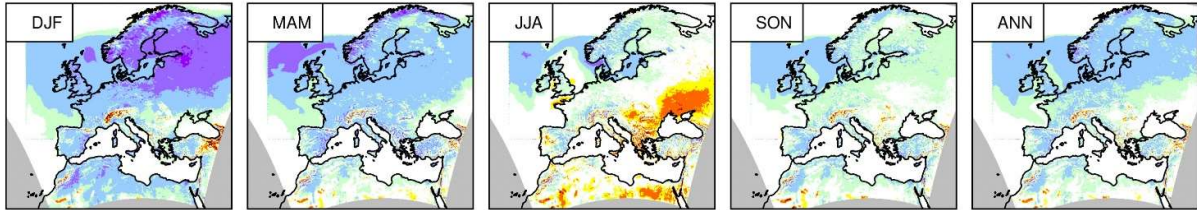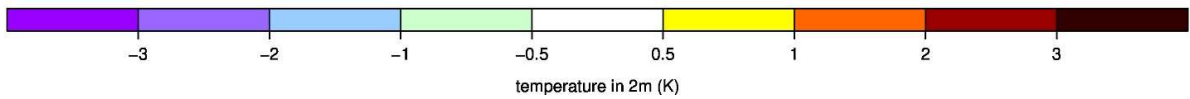
Figure 6: Seasonal (DJF, MAM, JJA, SON) and annual (ANN) mean of 2m air temperature (K) difference of a) ICON266, b) ICPL266 and c) ICPL266_flx to the ERA5 reanalysis data for the period of 2010-2018.
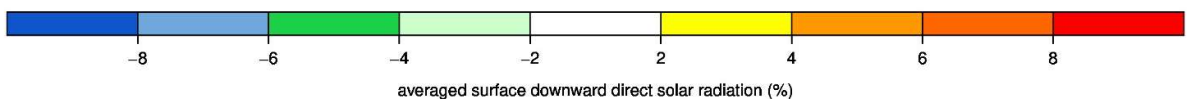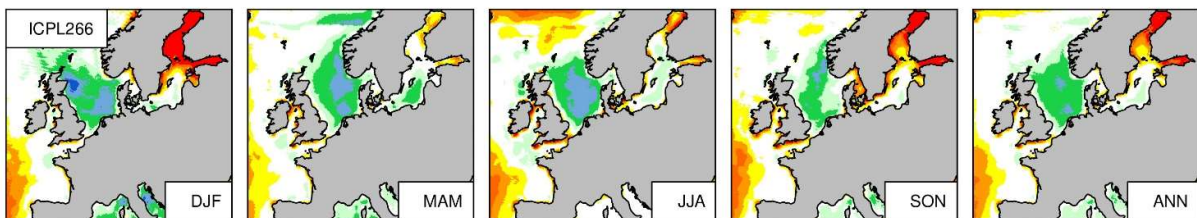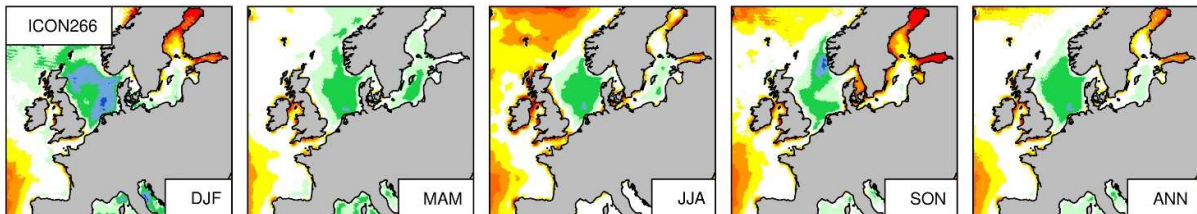
Figure 7: Seasonal (DJF, MAM, JJA, SON) and annual (ANN) mean of shortwave downward radiation bias (%) of ICON266 (top) and ICPL266 (bottom) compared to the ERA5 data for the period of 2010-2018 over the GCOAST domain.

28
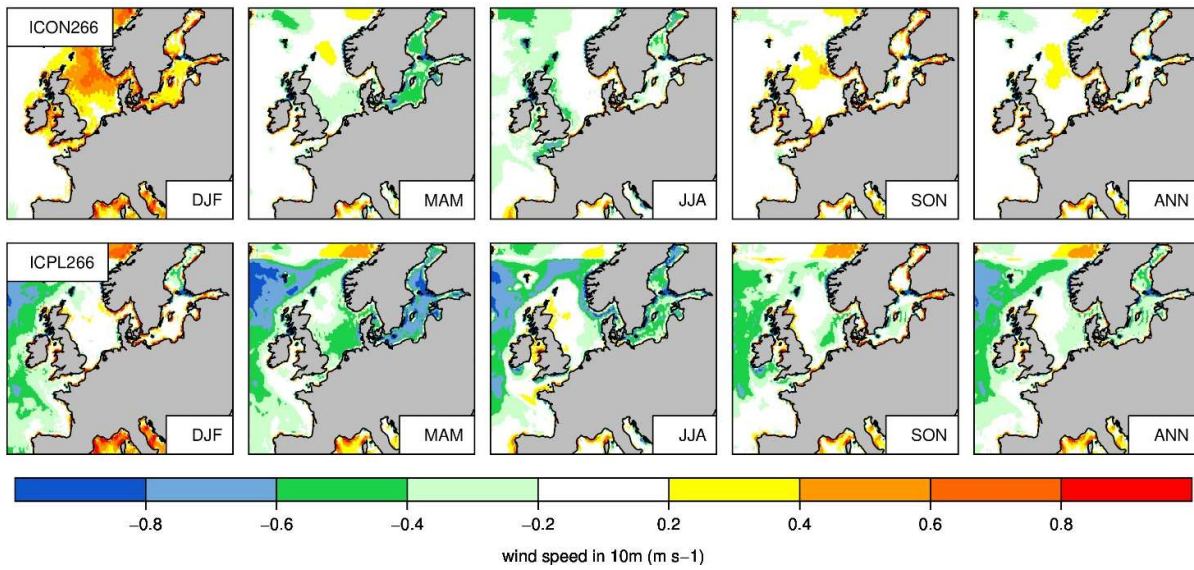
787
788 *Figure 8: Seasonal (DJF, MAM, JJA, SON) and annual (ANN) mean 10-M wind speed bias (m s $^{-1}$) of*
789 *ICON266 (top) and ICPL266 (bottom) compared to the ERA5 data for the period of 2010-2018 over*
790 *the GCOAST domain.*
791

792   a) ICON266

793
794   b) ICPL266

795
796   c) ICPL266_flx

797
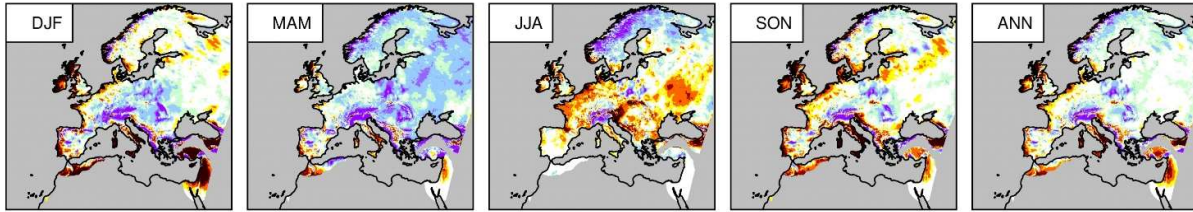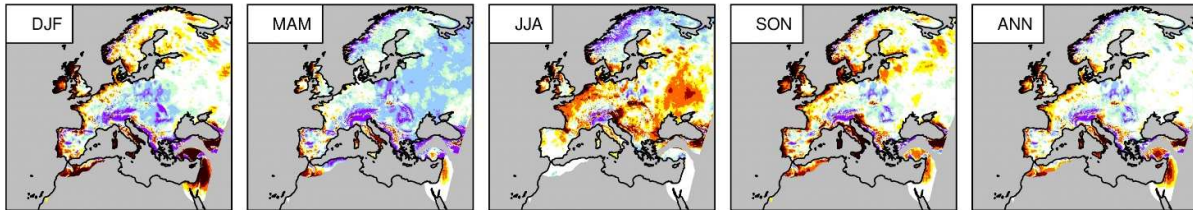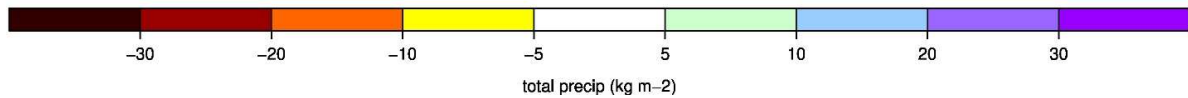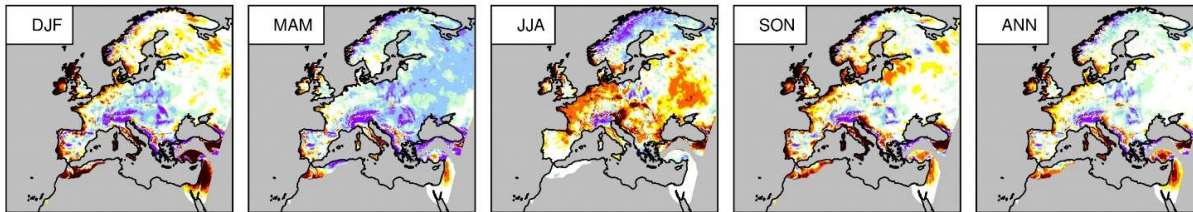
Figure 9: Seasonal (DJF, MAM, JJA, SON) and annual (ANN) difference of precipitation (mm month⁻¹) for a) ICON266, b) ICPL266 and c) ICPL266_flx compared to the E-OBS data for the period of 2010-2018.

798

a) Sea surface temperature | avg. GCOAST | ocean
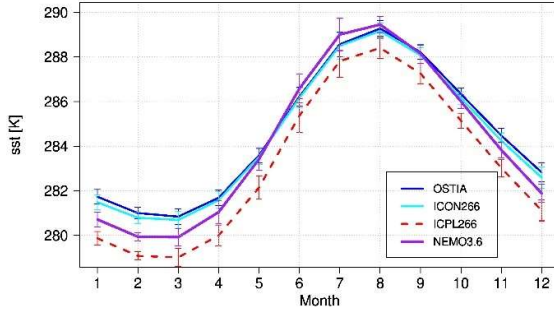
b) Precipitation | avg. GCOAST | land
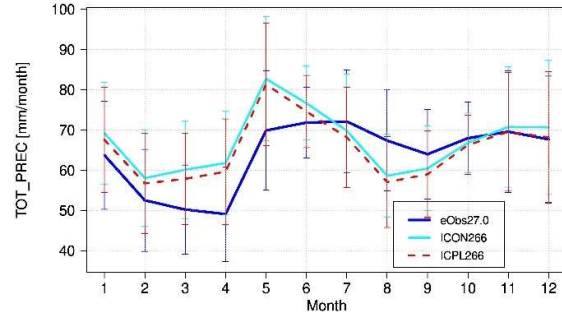
c) 2M air temperature | avg. GCOAST | ocean
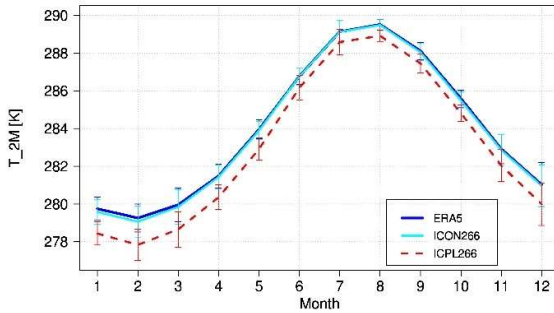
d) 2M air temperature | avg. GCOAST | land
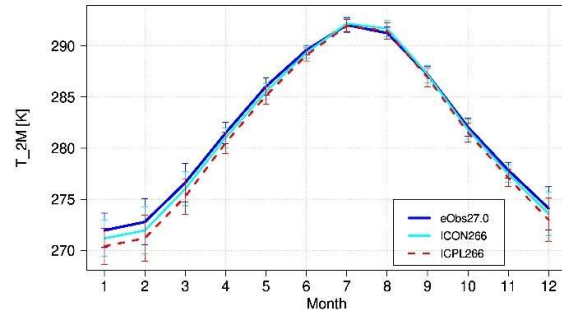
e) Mean sea level pressure | avg. all | ocean
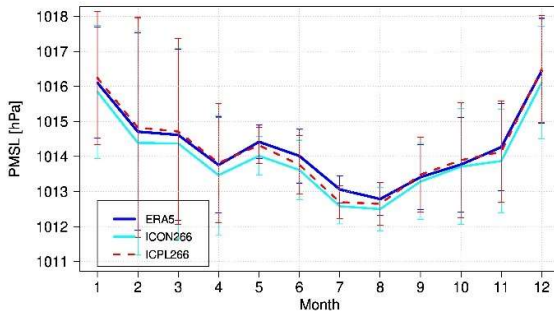
f) Mean sea level pressure | avg. all | land
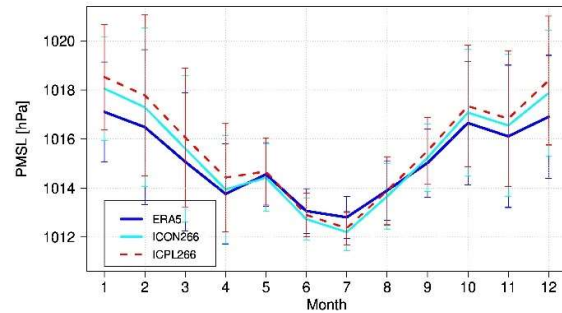
Figure 10: Climatological monthly mean of T_S (K), T_2M (K), PMSL (hPa) and precipitation (mm/month) of ICON266 (cyan solid line) and ICPL266 (red dashed line) compared to the OSTIA, ERA5 and E-OBS data (blue solid line) for the period of 2010-2018. a) includes also the SST of NEMO 3.6 (purple solid line) averaged over the GCOAST domain. Values are averaged over the GCOAST domain (avg. GCOAST) or the whole EURO-CORDEX domain (avg. all), over the ocean or land points only. The vertical bars show the standard deviation of the area mean data.
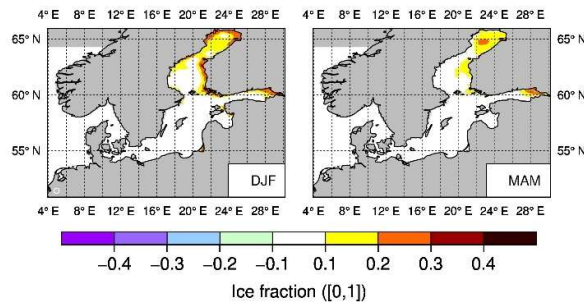
a) Sea ice fraction bias, ICPL266
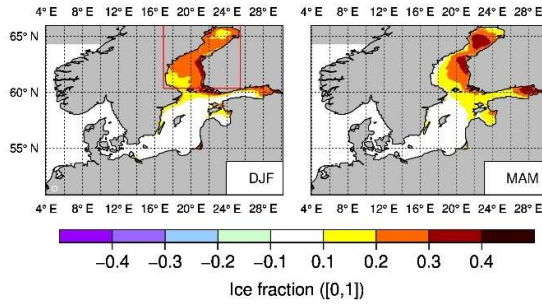
b) Sea ice fraction bias, ICPL266_flx
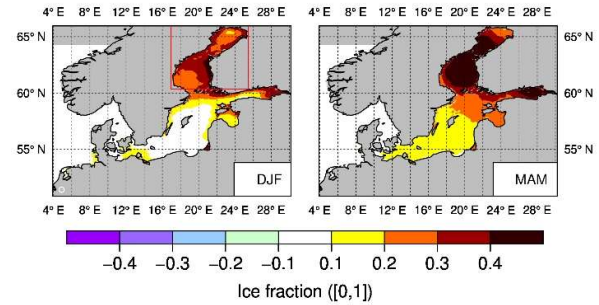
c) Sea ice fraction bias, NEMO3.6
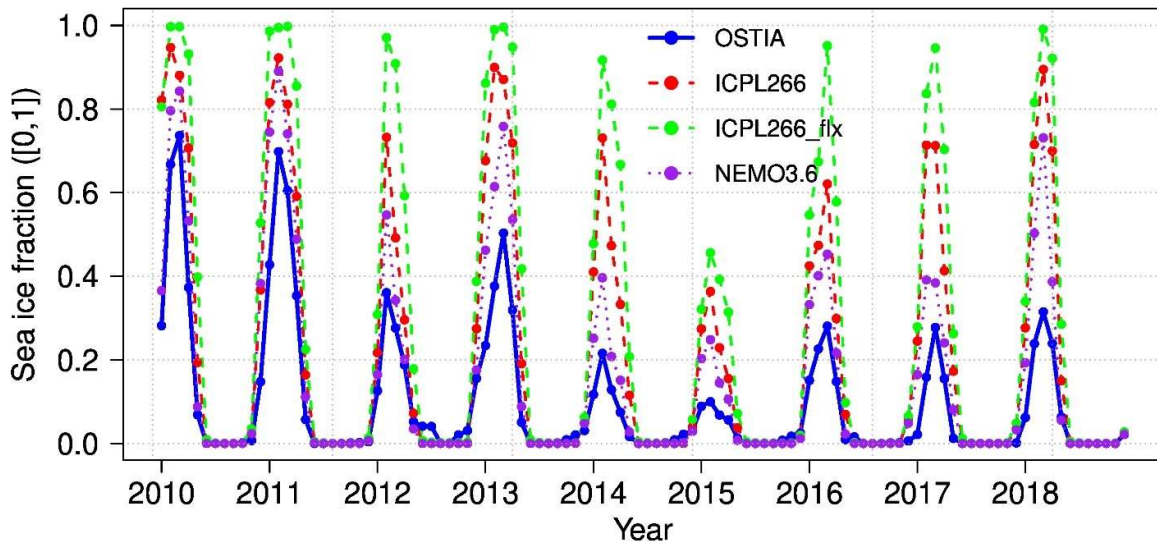

d) Sea ice fraction, Bothnian Bay & Sea

Figure 11: Sea ice fraction bias of a) ICPL266, b) ICPL266_flx, c) NEMO3.6 compared to the OSTIA data in winter (DJF) and spring (MAM) averaged over the period of 2010-2018; d) Monthly mean of sea ice fraction averaged over the Bothnian Bay & Sea (red box in Fig. 11a) of OSTIA, ICPL266, ICPL266_flx and NEMO3.6 during 2010-2018.
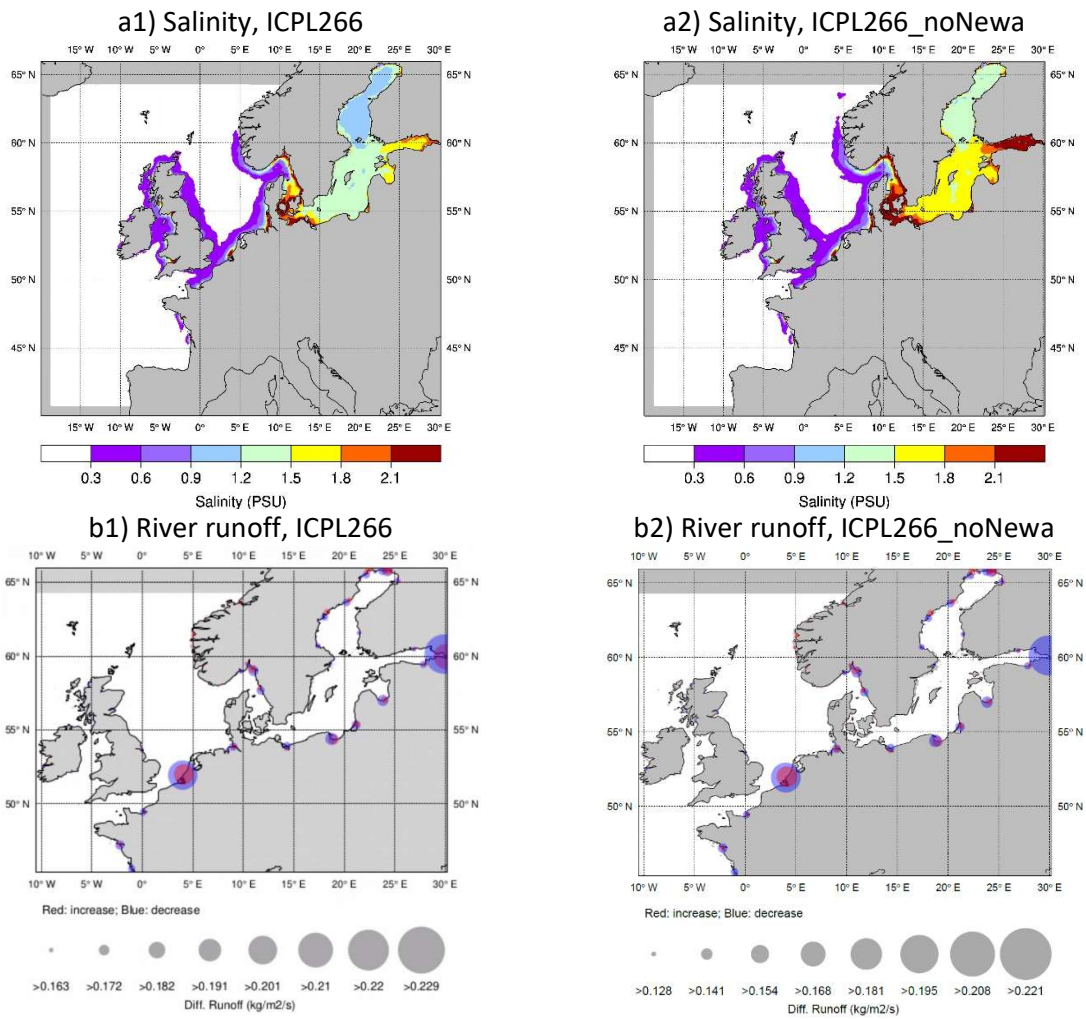
807

Figure 12: a1) Salinity difference (PSU) and b1) river runoff difference (kg/m2/s) between ICPL266 and NEMO3.6 averaged over the period of 2010-2018. a2) and b2) salinity and river runoff difference of ICPL266_noNewa compared to NEMO3.6. In Fig. 12 b1 and b2, the size of the grey circles indicates the magnitude of the positive (red color) and negative (blue) differences.

808